Modelling ballast via a non-linear lattice to assess its compaction behaviour at railway transition zones

de Oliveira Barbosa, J.M.; Faragau, A.B.; van Dalen, K.N.; Steenbergen, M.J.M.M.

DOI
10.1016/j.jsv.2022.116942

Publication date
2022

Document Version
Final published version

Published in
Journal of Sound and Vibration

Citation (APA)
de Oliveira Barbosa, J. M., Faragau, A. B., van Dalen, K. N., & Steenbergen, M. J. M. M. (2022). Modelling ballast via a non-linear lattice to assess its compaction behaviour at railway transition zones. *Journal of Sound and Vibration*, *530*, 116942. Article 116942. https://doi.org/10.1016/j.jsv.2022.116942

Journal of Sound and Vibration 530 (2022) 116942

Contents lists available at ScienceDirect

Journal of Sound and Vibration

journal homepage: www.elsevier.com/locate/jsvi

Modelling ballast via a non-linear lattice to assess its compaction behaviour at railway transition zones

João M. de Oliveira Barbosa [a], Andrei B. Fărăgău [b], Karel N. van Dalen [b,*], Michael J.M.M Steenbergen [a]

[a] *TU Delft, Faculty of Civil Engineering and Geosciences (CiTG), Department of Engineering Structures, Section of Mechanics and Physics of Structures. Stevinweg 1, 2628 CN Delft, The Netherlands*

[b] *TU Delft, Faculty of Civil Engineering and Geosciences (CiTG), Department of Engineering Structures, Section of Dynamics of Solids and Structures. Stevinweg 1, 2628 CN Delft, The Netherlands*

ARTICLE INFO

Keywords:
Track degradation, Ballast settlement, Transition, Non-linear lattice, Support stiffness variation
non-linear lattice, support stiffness variation

ABSTRACT

Locations in railway tracks where significant variations of the track properties occur are subject to increased track deterioration. To successfully mitigate this, the mechanisms leading to the increased deterioration need to be understood. To this end, this work presents a non-linear constitutive law for a lattice model able to describe the compaction behaviour of railway ballast. The parameters of the non-linear connections are tuned against lab experiments of cyclic loading tests and direct shear tests. The tuned lattice can be used with different foundation properties provided that the ballast in the track is equivalent to that of the tests. The non-linear lattice model is applied to the case of railway transitions, for which ballast compaction under train loading is studied as a cause of geometry degradation. It is observed that for the studied cases of a culvert crossing and of a ballast-slab transition, the operation-induced compaction converges monotonously to a stable situation, without leading to significant changes in the vehicle-track interaction. Ballast compaction is therefore insufficient as a stand-alone mechanism to explain a process of progressive degradation of the track geometry. Other mechanisms like autonomous differential settlement at the foundation level must be taken into account in such cases.

1. Introduction

It is well established in the literature that zones where railway tracks exhibit changes in cross-sectional properties along the longitudinal direction are subject to increased track deterioration, which in turn leads to more frequent maintenance operations [1,2]. Such changes can take the form of stiffness variations in the foundation (for example, when the track passes over a rigid structure, like a culvert), transitions from ballasted to ballastless (slab) tracks, or even transitions from open track to civil structures (like bridges and tunnels). There is no complete physical understanding as yet of the accelerated degradation, but some causes are pointed out by different researchers [3–6]: i) a dynamic amplification of the track response due to longitudinal variations (e.g., stiffness variation) causes faster degradation; ii) increased degradation leads to an unlevel rail profile causing further amplifications (negative feedback loop); iii) due to presence of structures, the autonomous settlement of the foundation (soil consolidation, for example) may differ

---

* corresponding author.
E-mail address: k.n.vandalen@tudelft.nl (K.N. van Dalen).

https://doi.org/10.1016/j.jsv.2022.116942
Received 20 August 2021; Received in revised form 21 March 2022; Accepted 1 April 2022

between the open track and the part with the structure, which amplifies the feed-back loop described in ii). Indicators of track degradation are the increasingly unlevelled vertical position of the track, the occurrence of hanging sleepers, damage to the sleepers, ballast crushing, and others [3]. In order to design efficient mitigation solutions to this problem, it is important to understand the primary causes driving the localised deterioration of the track. Within this framework, the present work focuses on understanding if the vertical compaction of ballast can be responsible, as a stand-alone mechanism, for cases of progressive loss of vertical geometry of an initially straight track due to differential settlement. By progressive, the negative feedback loop is meant, where the settlement leads to increased forces leading in turn to more settlement. To that aim, a non-linear lattice model for ballast is presented.

Ballast behaviour has been a subject of multiple studies, including field measurements and condition monitoring [7–9], lab experiments ranging from small scale [10,11] to real scale [12–14], and numerical simulations based on DEM (discrete element method) [15–21]. An important observation is that under cyclic compressive loading ballast particles rearrange in the granular matrix, leading to a cumulative densification of the layer, resulting in gradual settlement along with stiffening of the global medium. The rate and maximum value of settlement depends on the boundaries of the medium (confining or not), the amplitude of the applied load, the stage of the process and the initial densification of the matrix, the grading (sieve curve) of the ballast particles, and the particle shape, which in turn depends on factors like fresh versus recycled, number of tamping operations, etc. If the amplitude of the applied load is high enough, particle crushing may occur, especially in the load-bearing path of concrete sleepers, which leads also to a gradual change of the grading distribution and of the porosity/drainage properties of the ballast layer. Some lab tests have shown that the accumulated settlement under constant loading amplitude can reach 1 cm after half dozen millions of cycles [13].

The understanding of ballast behaviour gained through lab experiments and numerical simulations has been transferred to models of the railway track. Researchers formulated simplified ballast models that can be used in 1D track models [e.g., 22]. One-dimensional models have been used to study, for example, transition radiation and the effect of non-linearities [23–25], and also how the system responds in the case of hanging sleepers [26–28]. When it comes to capturing ballast settlement over time have, a multitude of empirical or phenomenological models have been proposed: logarithmic model [29], Shenton model [30], Sato model [31], Hettler model [32], and more recent ones [e.g., 33]; detailed overviews of these models can be found in Refs. [33,34]. Although 1D models are fast to solve and require a relatively low level of accuracy in the representation of the substructure, they are also simplistic, limiting their applicability to describe phenomena related to the substructure and optimize the geometry and composition of the substructure.

Multi-dimensional models, mostly based on FEM (finite element method), are more versatile [35–37]; they can model any geometry, material type and accuracy level, but they require significant computational power (especially 3D), which makes them unsuitable for more than a few axle passages, especially when the boundaries of the modelled domain are placed far from the region of interest. Nonetheless, under certain assumptions and simplifications, researchers have simulated accumulation of ballast settlement using multi-dimensional continua. Suiker et al. [35] developed a ballast model that captures accumulation of settlement using a continuum in a 2D FEM framework. In a similar framework, Indraratna et al. [38] used the so-called hardening-soil model for the ballast settlement. Recently, Shih et al. [39] considered a 3D description of a small part of the railway track where an extended Drucker-Prager plasticity model was used for ballast settlement. However, these models have only considered a transverse cross-section of the railway track [35,38] or a limited portion of the railway track in longitudinal direction [39] (i.e., no transition zones or actual moving vehicles) making them closer to lab experiments than to modelling railway-track dynamics at transition zones. Another category of 2D [40] and 3D [36,37] FEM models is simulating the ballast settlement indirectly through empirical models (like the ones explained for the 1D models); the ballast constitutive law used in the track models can be assumed linear or nonlinear-elastic and the accumulation of settlement is imposed through empirical models based on the stresses/strains computed; every few thousands of cycles in the empirical model, the stresses/strains are re-computed using an updated profile of the track, to determine the further evolution of the settlement. This appears to be the most advantageous solution that is found in the literature for combining the complex dynamic behaviour of the vehicle-track-soil interaction with a changing geometry due to accumulation of ballast settlement. Nonetheless, the settlement is accounted for through empirical models; consequently, specific physical phenomena occurring in the process of settlement (such as phenomena at a granular level) cannot be investigated and their explicit influence on the dynamic track response is not accounted for.

A third small and recent category of models simulate ballast settlement using DEM as part of a small portion of a railway-track model containing, for example, 3 sleepers [19,41,42] or 10 sleepers [21]. Such a combination (railway track model with DEM for ballast) can potentially lead to the most accurate predictions. However, due to the computational cost, the track model has to be of very limited size. This makes an investigation that includes the railway track together with a transition zone practically impossible.

Within the framework of multi-dimensional models, recently the authors proposed a 2D model of a railway track (including transitions) in which the behaviours of ballast and soil are simulated via regular linear lattices [43,44], and in which the infinite character of the track is intrinsically accounted for, allowing to reduce the dimension of the modelled region. Besides the computational gains due to reduction of the model size, the fact that a lattice is used is another aspect distinguishing the proposed model from others that are typically based on a classical continuum. The latter cannot correctly predict wave propagation at high frequencies in granular media, and neither can it accurately describe deformations when the length scale of variation is in the order of the ballast particle size [45]; such deformations are, however, expected at the edges of the sleeper-ballast interface, where localized slide leads to neighbouring particles undergoing very different deformations. Therefore, considering the three categories of models previously presented, the model proposed here, which is an extended version of the one proposed in [43,44], aims to combine the strengths of the second and third categories; namely, to use the multi-dimensional framework that accounts for the vehicle-structure-soil interaction at transition zones (strength of the second category) together with modelling the discrete nature of the ballast, the settlement mechanisms as well as their explicit influence on the dynamic response (i.e., without using empirical models for ballast settlement; strength of the third category).

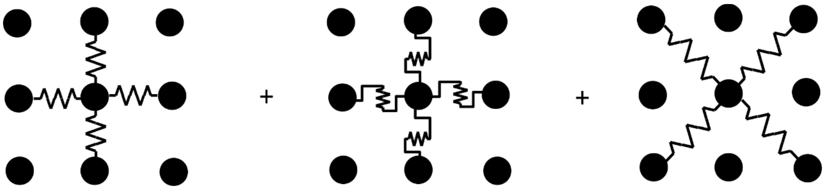

Figure 1. Contacts between particles. Axial normal (left), axial shear (middle) and diagonal normal (right).

The goals of the present work are to (i) define a non-linear model for the lattice representing the ballast layer, and (ii) use it to evaluate and assess the differential settlement of ballast caused solely by parameter variations in the longitudinal direction of the track at transition zones. When it comes to (i), the non-linear lattice is defined such that its properties are tuned against lab tests of ballast layers under cyclic vertical loading [13], resulting in a phenomenological model that can be applied for distinct support conditions and transition types. To accomplish (ii), the cause of differential settlement to be investigated in this work (i.e., parameter variations in longitudinal direction) is isolated from all other settlement causes (a-priori unlevel rail, a-priori hanging sleepers, autonomous settlement of the subgrade, etc.) The model that results from this work is versatile, can consider different types of trains, moving speeds, initial conditions of the track (like unlevelled rails and hanging sleepers, although these are not incorporated in this work), longitudinal changes and transitions in the foundation, and different ballast properties (tuned to lab experiments, including potential mitigation measures like binding polymers [46]). The model can be used to assess how the vertical geometry of the track changes after each train passage, whether that process converges or not, how the train-track interaction forces change throughout time, and if hanging sleepers may occur or not.

This manuscript is organized as follows. Section 2 describes how ballast compaction is modelled via non-linear behaviour of the connections in the lattice. In Section 3, the lattice is further improved in order to simulate also shear failure. In Section 4, the procedure to solve the time domain equations that result from considering the lattice inertia and viscous damping is explained. In Section 5, the non-linear lattice is used to assess the evolution of track settlements due to ballast compaction for two types of transitions: a culvert passing underneath the railway track (based on a real stretch of the Dutch network) and a transition from ballasted track to slab track. In the last section, Section 6, the work is summarized and final considerations are presented.

2. Modelling compaction

The process leading to ballast settlement is compaction of the matrix by rearrangement of the particles [33]. On a local scale, compaction is a result of volumetric reduction and a consequence of the rearrangement of the ballast particles, which happens due to local shear failure and sliding at their contacts. The rearrangement of particles is a geometrically non-linear phenomenon, which leads to changes in the number and location of particle contacts, and to changes on how forces are transmitted throughout the matrix. In this work, however, particles are lumped up (from 3D to 2D) and it is assumed that the contacts between particles and their orientations remain unchanged during the calculations, even if the relative position of the particles may change. This entails that particle migration across the layer interfaces (e.g., from ballast to sub-ballast), which is one possible settlement mechanism, is not explicitly accounted for. Therefore, to describe settlements, a non-linear constitutive law for contacts between particles is defined such that, in a global way, the compaction behaviour of the ballast layer is equivalent to the one observed in lab tests or measurements.

In accordance with the two works that preceded this one [43,44], the ballast layer is modelled as a lattice, with a geometry as explained by Suiker and co-authors [45,47]. It consists of a regular network of masses, equally spaced and distributed, whose contacts between neighbouring particles are represented by normal, shear and diagonal connections as depicted in Figure 1. The mapping between a liner elastic continuum (with Lame's parameters G and λ) and a discrete medium of this type is based on the following equations [45]:

$$\begin{cases} \lambda & = \dfrac{k_{\mathrm{normal}}^{\mathrm{lat}} - 3k_{\mathrm{shear}}^{\mathrm{lat}}}{2d} \\ G & = \dfrac{k_{\mathrm{normal}}^{\mathrm{lat}} + k_{\mathrm{shear}}^{\mathrm{lat}}}{2d} \\ k_{\mathrm{diag}}^{\mathrm{lat}} & = \dfrac{k_{\mathrm{normal}}^{\mathrm{lat}} - k_{\mathrm{shear}}^{\mathrm{lat}}}{2} \end{cases} \tag{1}$$

Since the loading is, for the applications in question, in accordance with the gravity field (downwards), compaction leads to progressive lowering of the upper surface of the ballast layer. This behaviour can be simulated by shortening the relative distance between grains at consecutive vertical levels, a motion which is counteracted by the three elements shown in Figure 1 (but mostly the vertical axial springs and the diagonal springs). In this work, it is decided to simulate the non-linear behaviour of compaction via the vertical axial connections, even though in principle that could be achieved by using the full set of elements. Moreover, since the composition of the ballast layer is random on a local scale, the behaviour is expected to be similar when loaded horizontally or vertically, and therefore the horizontal axial connections are assigned the same properties as the vertical ones. The remaining connections (the shear connections, represented in the middle panel, and the diagonal connections, represented in the right panel) will be

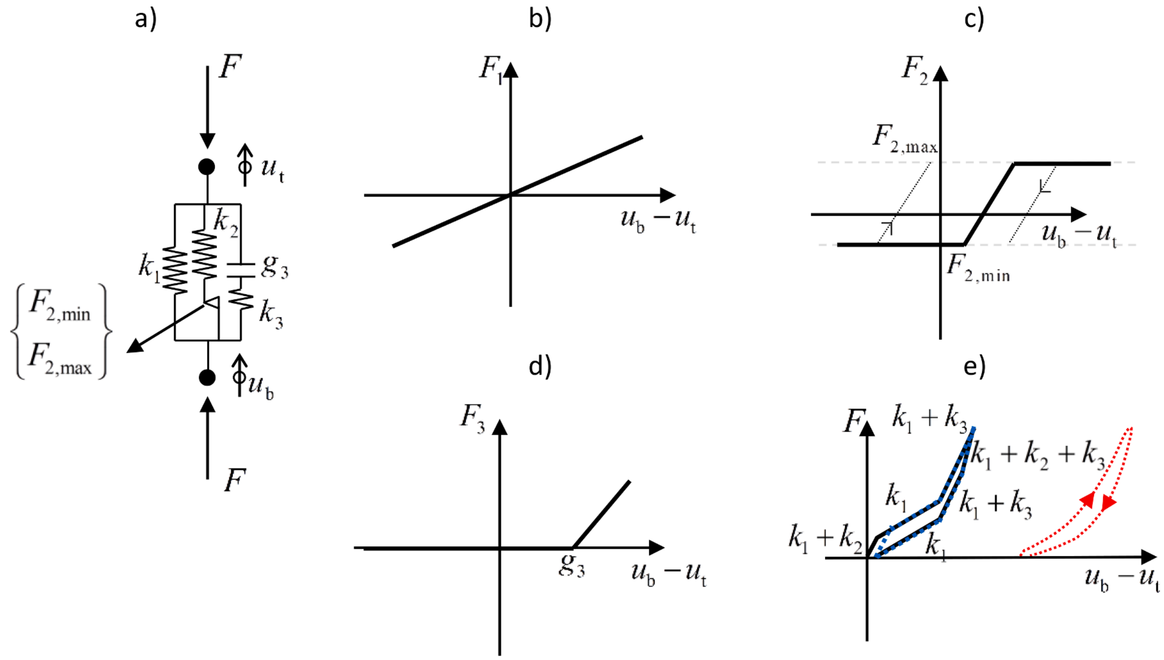

Figure 2. Normal connection aiming at reproducing the compaction behaviour of ballast. a) Connection as a parallel assembly of a linear spring, a spring-slider couple, and a spring-gap couple; b) force-displacement relation for linear spring; c) force-displacement relation for spring-slider couple (the offset with respect to the vertical axis represents an arbitrary slide; the dotted diagonal lines represent potential paths after resistance is regained); d) force-displacement relation for spring-gap couple; e) first (black) and second (dotted blue) load/unload cycles of the proposed normal connection, and sketch (dotted red) of a generic load-unload cycle of cyclic compaction tests.

used to reproduce other non-linear behaviour of ballast, and that is discussed in the next section.

There are four main features of compacting ballast that the non-linear connection must take into account. These are: i) the successive increment of vertical displacement; ii) the load dependent settlement, i.e., the maximum settlement depends on the maximum load amplitude [12,48]; iii) the increase of the vertical stiffness [10,13]; iv) the inability to transmit tensile forces (which is a general property of unbound granular material). These are the only features that are incorporated explicitly in the lattice model; therefore, all other features/mechanisms of ballast compaction (particle breakage, lateral spreading of ballast, etc.) are implicitly incorporated only if the experiments to which the model is fitted have accounted for these mechanisms. Furthermore, because the lattice is an idealized representation of the ballast through a geometrically-regular structure, the particle size is chosen as the median diameter of the ballast sample to which it is tuned. As the constitutive behaviour of a granular matrix depends on the actual particle size distribution/sieve curve, this is accounted for implicitly through the tuning of the model.

To model features i) to iv), the connection depicted in Figure 2a is proposed. It consists of a linear spring (with elastic constant k_1) in parallel with a spring-slider couple (elastic constant k_2 and minimum and maximum forces $F_{2,\min}$ and $F_{2,\max}$) and with a spring-gap couple (elastic constant k_3 and gap g_3; until the gap is filled, this couple carries no load). The spring-slider couple has stick-slip behaviour, i.e., if the minimum(maximum) force is reached, the slider is activated and the couple can elongate(shorten) freely until the bearing force is increased(reduced), at which moment the couple sticks and regains resistance to deformation. To comply with condition iv), the total force carried by the three components is imposed to be non-negative. The force-displacement relations for each of these three components are represented in Figure 2b-d, and the force-displacement relation during one loading and unloading cycle that results from coupling these three components is represented in Figure 2e. The load-unload cycle is, in some way, similar to the ones obtained during cyclic compression loading of granular material (a sketch is depicted by the red line in Figure 2e – colours only visible in online version); in these tests, during loading the sample exhibits a brief softening behaviour followed by a stiffening trend, and during unloading exhibits gradual softening [49].

At the end of the first load cycle, the connection exhibits residual deformation that originates from the sliding at the spring-slider couple. If loaded a second time with the same load amplitude (the second loading path is represented with blue dotted line in Figure 2e), the maximum shortening of the connection will be the same as in the first load, and after unloading, the final residual deformation will also remain the same. This does not comply with the first feature mentioned in the previous paragraph, since for a constant load-unload amplitude, the maximum residual deformation is obtained at the first cycle and not gradually. To allow for further accumulation of residual deformations, the properties of the slider must be changed in such a way that it starts sliding while carrying lower loads, i.e., the sliding force $F_{2,\max}$ must be reduced from one load cycle to the next (physically, this can correspond to the reduction of friction between two particles due to relative sliding and consequent abrasive wear and smoothening of the contact surface). Therefore, every time the force carried by the spring-slides couple reaches $F_{2,\max}$, after that force starts decreasing and the

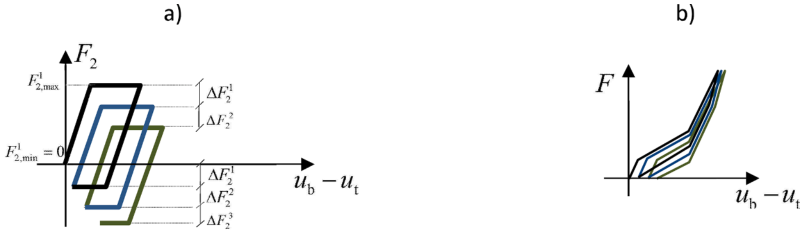

Figure 3. First (black), second (blue) and third (green) load/unload cycles. a) Force-displacement relation of spring-slide couple. b) Force-displacement relation of proposed connection, after introducing slide force reduction.

couple regains resistance, and when the carried force has reduced more than a certain threshold ΔF_2, the maximum force $F_{2,\max}$ is lowered by that amount; the minimum resistance force $F_{2,\min}$ is also reduced by the same amount. This leads to the definition of cycle dependent sliding forces $F^i_{2,\max}$ and $F^i_{2,\min}$of the type (see Figure 3a)

$$\begin{aligned} F^{i+1}_{2,\max} &= F^i_{2,\max} - \Delta F^i_2 \\ F^{i+1}_{2,\min} &= F^i_{2,\min} - \Delta F^i_2 \end{aligned} \tag{2}$$

where the superscript i represents the cycle number, and ΔF^i_2 is the sliding force reduction, which is cycle dependent. With this cycle dependency of the sliding forces, the consecutive load-unload cycles now lead to accumulative residual deformation, as depicted in Figure 3b.

The initial values $F^1_{2,\max}$ and $F^1_{2,\min}$ must be defined by the user in such a way that, together with the remaining parameters of the connections, the simulated load-unload behaviour resembles that of lab tests. The authors suggest $F^1_{2,\min}=0$, and based on that choice, the residual deformation r^i at the end of cycle i can be calculated with the following expression (assuming that the variation ΔF^i_2 is small enough for slide to occur again during unloading):

$$\begin{cases} r^i = \dfrac{-F^{i+1}_{2,\min}}{k_1} = \dfrac{-F^i_{2,\min} + \Delta F^i_2}{k_1}, & r^i < g_3 \\ r^i = \dfrac{k_3 g_3 - F^{i+1}_{2,\min}}{k_1 + k_3} = \dfrac{k_3 g_3 - F^i_{2,\min} + \Delta F^i_2}{k_1 + k_3}, & r^i > g_3 \end{cases} \tag{3}$$

The slide force variation ΔF^i_2 shall be defined such that the features mentioned in the beginning of this section are respected. Hereto, the dependency of the settlement on the applied force must first be established [12]. Here, it is assumed that the maximum achievable settlement $s_{\lim}$ (assuming constant load amplitude) varies linearly with the applied load amplitude F according to the following law:

$$s_{\lim} = \frac{\min\{F, F_{\max}\} - F_{\min}}{F_{\max} - F_{\min}} s_{\max}, \; s_{\lim} \geq 0 \tag{4}$$

The variable $s_{\max}$ represents the maximum settlement that can be obtained (no matter how large the force is, there is a limited amount of void volume that the particles can use to rearrange themselves), $F_{\max}$ represents the force amplitude that leads to $s_{\max}$, and $F_{\min}$ represents the threshold force amplitude below which no settlement occurs. By establishing a parallel between expected settlement (observable quantity) and residual deformation (model), the following expression can be derived for the limit residual deformation $r^i_{\lim}$ as function of the load amplitude F^i:

$$r^i_{\lim} = \frac{\min\{F^i, F_{\text{ref}}\} - F^1_{2,\max}\frac{k_1+k_2}{k_2} - k_3 \max\left\{0, \frac{F^1_{2,\max}}{k_2} - g_3\right\}}{F_{\text{ref}} - F^1_{2,\max}\frac{k_1+k_2}{k_2} - k_3 \max\left\{0, \frac{F^1_{2,\max}}{k_2} - g_3\right\}} r_{\max} \tag{5}$$

Compared to Eq. (4), in the previous expression $F_{\min}$ is replaced by $F^1_{2,\max}\frac{k_1+k_2}{k_2} + k_3 \max\left\{0, \frac{F^1_{2,\max}}{k_2} - g_3\right\}$, which is the minimum force needed for sliding to occur the first time. Also, in Eq. (5), $r_{\max}$ represents the maximum residual deformation allowed for the connection (to be defined by the user) and F_{ref} represents the load amplitude that leads to that residual deformation (also to be defined by the user); these two quantities relate directly to $s_{\max}$ and $F_{\max}$[1]. By enforcing that the residual deformation at end of cycle i - Eq. (3) – is not larger than the limit residual deformation given by Eq. (5), a limit is obtained for the slide force reduction:

---

[1] For example, if the ballast sample is to be modelled with a single element, then $r_{\max} = s_{\max}$ and $F_{\text{ref}} = F_{\max}$ (see Section 2.1); if ballast is to be modelled with a lattice, then the maximum allowed settlement $s_{\max}$ and the maximum force $F_{\max}$ must be distributed over the different connections (see Sections 2.3 and 3.1).

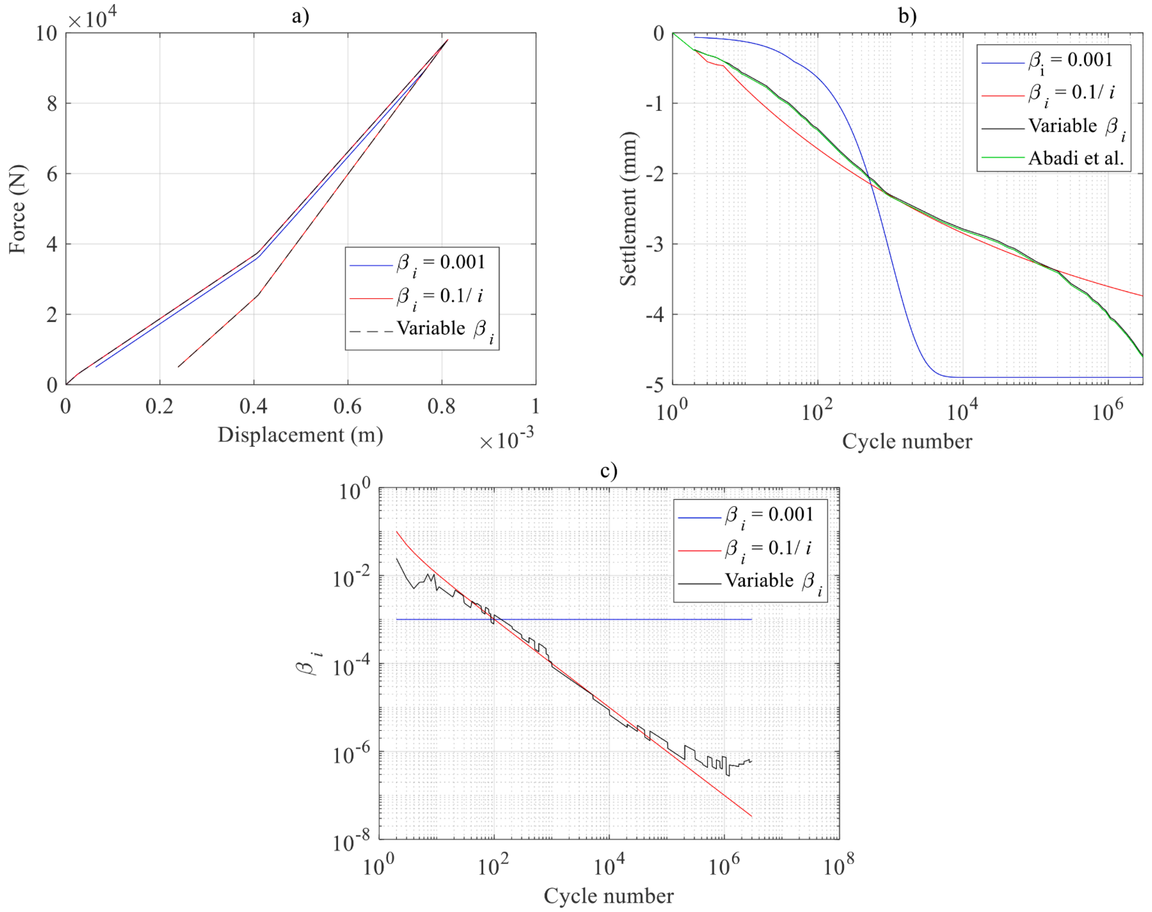

Figure 4. Cyclic response of the non-linear connection. a) Force displacement relationship for the first load-unload cycle. b) Settlement at the end of each load cycle. c) Sliding force reduction ratio.

$$\Delta F_2^i \leq r_{\text{lim}}^i k_1 + k_3 \max\left\{0, r_{\text{lim}}^i - g_3\right\} + F_{2,\text{min}}^i \tag{6}$$

If the slide force reduction assumes its maximum value, the maximum residual deformation is attained after one cycle, and that contradicts the feature of gradual increase of settlement. Thus, the actual force reduction should be only a fraction of its maximum value, and thus can be defined as

$$\Delta F_2^i = \beta_i \left(r_{\text{lim}}^i k_1 + k_3 \max\left\{0, r_{\text{lim}}^i - g_3\right\} + F_{2,\text{min}}^i \right) \tag{7}$$

where the degradation-rate coefficient β_i must be defined by the user, and should be between 0 (meaning that no settlement accumulation occurs) and 1 (meaning that settlement stabilizes after one load cycle). Coefficient β_i dictates the speed of the compaction; the higher β_i, the fewer cycles are needed to reach the final compaction. For general purposes, this coefficient needs to be tuned against experiments such that the rates of compaction match. More restrictions for β_i can be imposed by the specific scenario to be simulated. For example, for scenarios where hundreds of thousands of cycles (usually the ballast settlement stabilizes after a large number of cycles) cannot be simulated, β_i can be artificially increased such that the settlement stabilizes after fewer cycles, if one is interested in the final configuration and not in the exact evolution.

2.1. Cyclic loading of ballast – simulation with one non-linear element

A single element corresponding to the non-linear connection defined above is used next to simulate the cyclic loading of ballast layers. In the literature, there are several reports of laboratory cyclic loading tests on ballast, ranging from small-scale box tests [10] and track tests [11], to full-scale tests in which the subgrade may [12,14] or may not [13] be included. Though initially the small-scale box tests were used as reference, it became evident that when scaling up the results to real conditions the observations were unrealistic, partly due to the lack of pre-compaction of the ballast sample and partly due to inadequate lateral constraint of the ballast sample, and therefore it was decided to use instead the results from Abadi and co-authors [13]. In their tests, the authors subjected a ballast sample (corresponding to one sleeper bay) to a vertical force whose amplitude varied harmonically between 5 kN and 98.1 kN, and registered the settlement at the end of each load cycle (at 5 kN). The force was applied on two sections of UIC60 rails – left and right – which were supported by a monoblock G44 sleeper whose base dimensions were 2.5 m by approximately 0.3 m; the sleeper bay was 0.65 m long, and the thickness of the ballast layer under the sleeper was 0.3 m.

Several ballast types, with distinct granulometry, were tested; here the sample labelled 'Variant 3', whose median particle diameter is 0.03 m, is taken as reference. For this ballast type, the reported settlement after 4 million cycles is 0.0073 m (0.0024 m after the first load cycle), and the vertical stiffness of the ballast layer is reported to have varied from 120 MN/m (at the beginning of the experiment) to 150 MN/m (at the end of the experiment). Based on the mentioned values, the following parameters of the non-linear connection are quantified: $F_{\text{ref}} = 98100$ N; $r_{\max} = 0.0049$ m (final settlement offset by the settlement after the first load cycle). For the remaining parameters, the following conditions must be met:

(1) Initial stiffness: $k_s = k_1 + k_2 = 120 \text{ MN}/\text{m}$
(2) Final stiffness: $k_f = k_1 + k_3 = 150 \text{ MN}/\text{m}$
(3) Minimum force leading to settlement (slide of the spring-slide couple) – here, the authors assumed 3 kN, which corresponds roughly to the weight of a concrete sleeper and 0.60 m of two rails carried by each sleeper bay: $F^1_{2,\max}\frac{k_1+k_2}{k_2} + k_3\max\left\{0,\frac{F^0_{2,\max}}{k_2} - g_3\right\} = 3000$ N

There are three equations to determine five parameters: g_3, k_1, k_2, k_3 and $F^1_{2,\max}$. The best way to determine these five parameters is to tune them to the first and last load-unload cycles (force-displacement relationship) from lab experiments, in case these data are available. Because in the reference work (Ref. [13]) the load-unload paths are not described, here it is decided to add two more conditions to limit the number of combinations. These two conditions enforce that the first load path is similar to the one described in Figure 2e:

(1) The gap closed during the first loading: $\frac{F_{\text{ref}} - F^1_{2,\max}}{k_1} > g_3$
(2) First slide occurs before the gap is closed: $\frac{F^1_{2,\max}}{k_2} < g_3$

Based on the conditions (1)-(5), the following parameters are defined: $k_1 = 0.75k_s = 90 \text{ MN}/\text{m}$, $k_2 = 30 \text{ MN}/\text{m}, k_3 = 60 \text{ MN}/\text{m}, F^1_{2,\max} = 750$ N and $g_3 = 0.5F_{\text{ref}}/k_s = 0.00041$ m. Three situations are considered for the degradation-rate coefficient β_i, which controls how fast the residual deformation develops: in the first scenario, β_i is constant and equals $\beta_i = 0.001$; in the second scenario, β_i is cycle dependent and of the type $\beta_i = 0.1/i$; in the third scenario, β_i is such that the simulated settlement matches the settlement reported by Abadi et al. [13] (offset by the settlement after the first load cycle); for this last scenario, β_i is calculated from Eqs. (3), (5)-(7), by enforcing r^i. Figure 4 shows, for the three scenarios, (a) the first load-unload cycle, (b) the accumulated settlement over 3 million load cycles, and (c) the value β_i as a function of the cycle number.

As seen in Figure 4a, the loading path is the same for the three scenarios, and it contains the linear three stages depicted in Figure 2e (as imposed by conditions 4 and 5); the softening due to sliding happens at 3000 N (condition 3), and is subtly observed in the left bottom corner of the plot. The unloading path differs in the three scenarios, and that is caused by the different settlement allowed at the end of the first cycle; actually, the spring-slide couple starts sliding for the scenario in blue ($\beta_i = 0.001$), while it does not for the other two scenarios. This means that for $\beta_i = 0.1/i$ (red line) and for variable β_i (black line), the decrease in $F_{2,\min}$ (ΔF_2) is too large for sliding to occur again during unloading. That is, in fact, the reason why these two lines match.

As to the accumulated settlement, Figure 4b shows that it is possible to define cycle dependent values of β_i that reproduce the lab observations very accurately (black line vs green line). That value of β_i (black line) can be approximated reasonably well by the function $\beta_i = 0.1/i$ (red line) at least until the 200,000th load cycle, as shown in Figure 4c, and that is why the red line in Figure 4b follows closely the black and green lines until that load cycle, and thereafter diverges to slightly lower settlements. The constant value of $\beta_i = 0.001$ (blue line) does not capture the same evolution of settlements, being the development of settlements slower in the first 1,000 cycles and much faster afterwards, reaching the limit settlement imposed by the degradation law described in Eq. (7) before the 10,000 cycles.

For the reference cyclic test, the cyclic dependent $\beta_i = 0.1/i$ reproduces the results better than a constant β_i. However, the tests assumed a constant load amplitude, which is very specific, and so such approximation ($\beta_i = 0.1/i$, or similar) may not apply when the load is more generic and of random amplitudes, which is the case over the life span of a railway track (e.g., trains with different weights and speeds, hanging sleepers at transition zones leading to forces of impulsive nature on the ballast, etc.) For that reason, a constant value for β_i is preferred and assumed in the remainder of this work. For more realistic representation of settlement evolution under randomized loading, data for such conditions must be obtained, and only then expressions for β_i as function of load amplitude and cycle number can be attempted.

2.2. Load dependent settlement

Triaxial and cyclic tests show that the maximum plastic deformation of the ballast sample depends on the force amplitude that is applied [12,48]. In the proposed non-linear connection, that condition is accounted for via Eq. (7), which limits the sliding force

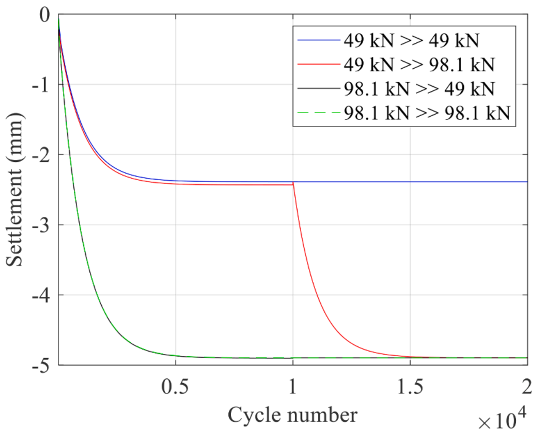

Figure 5. Accumulation of settlement for different load scenarios. The legend "$F_1 >> F_2$" describes the load scenario in which 10,000 cycles with load amplitude F_1 are followed by 10,000 cycles with load amplitude F_2.

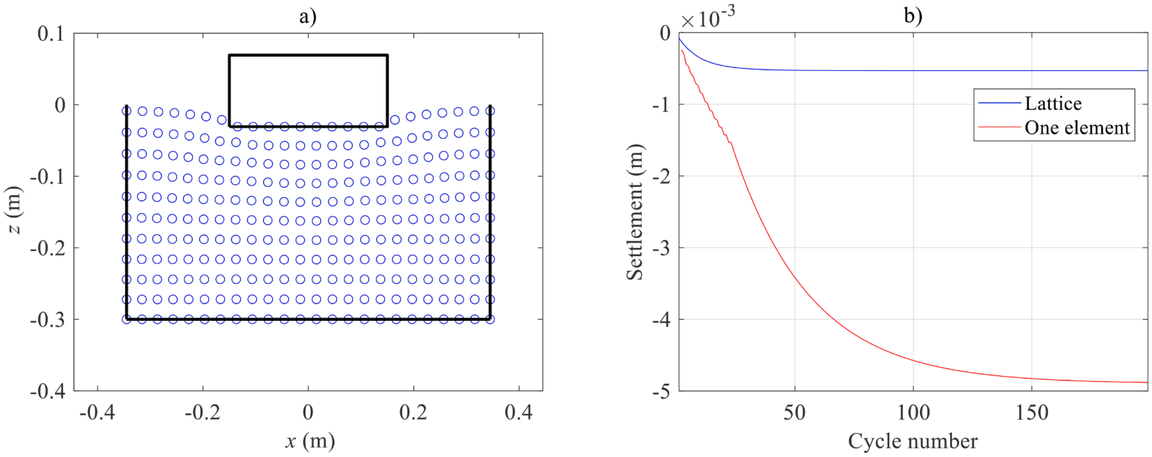

Figure 6. Response of the lattice due to the cyclic load. a) residual deformations at the end of the last load cycle (deformation is multiplied by 50 for visual purposes). b) Evolution of settlement at the end of each cycle (position of sleeper under the minimum load of 5 kN).

reduction ΔF_2. To test this functionality, the non-linear element defined in the previous subsection (with $\beta_i = 0.001$) is loaded with distinct load amplitudes and the evolution of the plastic deformation (settlement) is calculated. The plastic deformations are represented in Figure 5 as functions of the cycle number for the following load scenarios: i) 20,000 cycles with load amplitude of 49 kN (half of the force applied in the reference work; blue line); ii) 10,000 cycles with load amplitude 49 kN followed by 10,000 cycles with load amplitude of 98.1 kN (red line); iii) 10,000 cycles with load amplitude 98.1 kN followed by 10,000 cycle with load amplitude of 49 kN (black line); iii) 20,000 cycles with load amplitude 98.1 kN (green line). The figure shows that indeed the proposed non-linear connection is capable of limiting the plastic deformation based on the carrying force, as imposed by Eq. (6). In addition, the figure also shows that the maximum plastic deformation is load-path independent, i.e., the maximum accumulated residual deformation solely depends on the maximum force applied (provided that it undergoes enough cycles with that force) and not on the order with which the load amplitudes are applied; this feature is also observed in the triaxial tests. Qualitatively, the red line in Figure 4 is very similar to the results shown in Figure 14 of Ref. [12].

2.3. Cyclic loading of ballast test simulated with a lattice

Next, the cyclic test is simulated via a lattice. The diameter of the lattice particles is set at 0.03 m, which corresponds to the median particle diameter of the ballast sample tested in reference test [13]. Hence, the ballast is simulated with a lattice containing $N_x = 24$ columns and $N_z = 11$ rows of equally spaced masses, interconnected with springs as depicted in Figure 1. The vertical and horizontal normal springs are replaced with the non-linear connections defined in Figure 2. The edges of the lattice are constrained from moving in the direction perpendicular to the walls, and the $N_x^{\text{load}} = 10$ particles in the middle of the top row are prescribed to move vertically the same amount (simulating the sleeper) and are acted upon by a load which varies between 5 kN and 98.1 kN. See Figure 6a for a representation of the lattice and the boundary conditions.

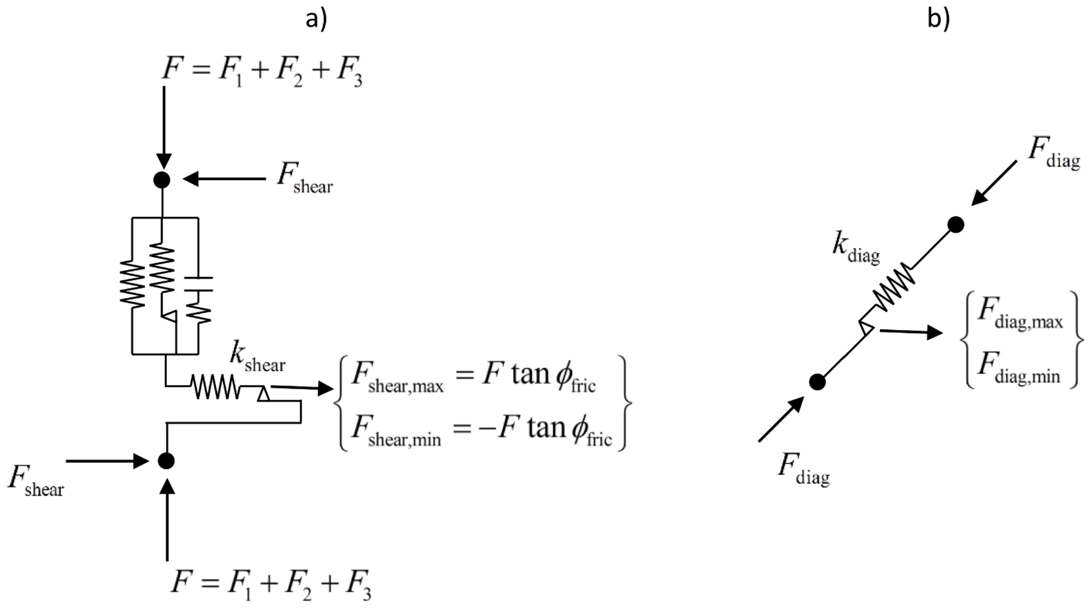

Figure 7. a) Stick-slip shear spring in series with “compaction” spring to simulate frictional resistance. b) Stick-slip diagonal spring to simulate apparent cohesion.

Because all particles are interconnected, the vertical stiffness must be spread through the connections under the sleeper. Hence, the lattice stiffnesses k_1^{lat}, k_2^{lat} and k_3^{lat} are set to $k_\alpha^{\text{lat}} = k_\alpha N_z / N_x^{\text{load}}$, where the values of k_α ($\alpha = 1, 2, 3$) are the values used in the previous subsection. Additionally, since the applied force is distributed over the several columns of particles under the sleeper, the maximum sliding force and reference force must also be adjusted, i.e., $F_{2,\max}^{1,\text{lat}} = F_{2,\max}^{1} / N_x^{\text{load}}$ and $F_{\text{ref}}^{\text{lat}} = F_{\text{ref}} / N_x^{\text{load}}$, and the gaps and maximum plastic deformations must be spread along the rows of the lattice, i.e., $r_{\max}^{\text{lat}} = r_{\max} / N_z$ and $g_3^{\text{lat}} = g_3 / N_z$. In what concerns the shear springs and the diagonal springs, for the current analysis they are assumed to behave linearly, and their stiffness values are set at $k_{\text{shear}}^{\text{lat}} = 0.1(k_1^{\text{lat}} + k_2^{\text{lat}})$ and $k_{\text{diag}}^{\text{lat}} = 0.45(k_1^{\text{lat}} + k_2^{\text{lat}})$. These values correspond to a Poisson’s ratio of 0.2, a value that is commonly used for ballast [47]. In addition, the value of β_i has been increased to $\beta_i = 0.03$ in order to reach faster a stabilized non-linear deformation (unlike the previous case, now with the lattice, the multiple degrees of freedom make it impractical to run tens of thousands of cycles).

Figure 6a shows the deformation of the lattice at the end of the 200th cycle, and Figure 6b shows the evolution of the settlement of the ballast layer, as seen from the top row of particles (which corresponds to the position of the sleeper; that is compared with the settlement as calculated with one element only, as in the previous sections). It is seen in Figure 6b that the obtained settlement is only 1/8 of the desired (0.6 mm instead of 4.9 mm); the reason for this lower settlement is the extra resistance offered by the diagonal and shear springs, which counteract the relative motion between particles, even if the normal connections have yielded completely. It can be expected that these connections also yield at some point, and that the resistance to the applied force is then mostly provided by the vertical normal connections between particles in between the sleeper edges (which does not happen in the current case, as seen in Figure 6a; there, the deformation of the surface spreads to the lateral boundaries of the lattice). This will be analysed in the next section, where the shear and diagonal springs are replaced by non-linear connections to simulate shear failure.

3. Shear failure

The main mechanism leading to ballast settlement is matrix compaction, which in turn is associated with the shear failure at the contact between particles. Explicitly modelling such local shear failure is a complex task that involves calculating contacts every time-step (contact location and contact forces). This is done in strategies like DEM [17], but is too computationally expensive for the current application. Consequently, the present model aims at replicating this mechanism only at a global level by allowing non-linear behaviour of the shear and diagonal connections.

The direct shear tests reported in work [50] are used as reference. In these tests, the authors filled two boxes with ballast particles, placed the boxes one on top of the other (with the free surfaces facing each other), applied a downward force on the upper box (which causes an equal reaction on the lower box), and then pushed laterally the lower box until failure was reached. Failure is understood as an increase of relative displacement between upper and lower boxes without increasing the lateral force. From the tests, the authors observed that for large enough values of the applied normal stress σ_{N} ($\sigma_{\text{N}} = F_{\text{N}} / A$; A is the area of the contact surface between the two boxes; F_{N} is the vertical force applied at the top box) the ultimate shear strength $\tau (\tau = F_{\text{H}} / A; F_{\text{H}}$ is the lateral force that leads to failure) depends linearly on σ_{N} according to the expression

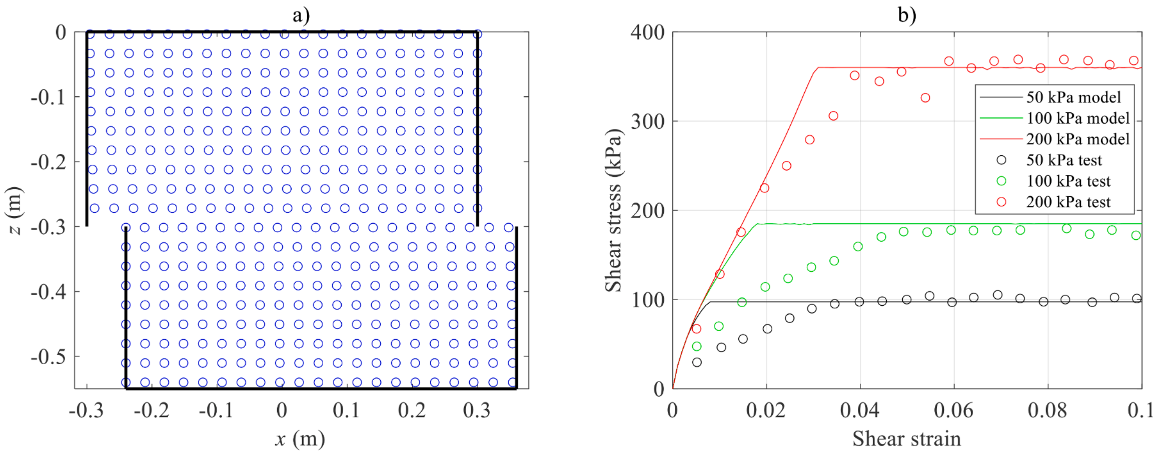

Figure 8. Lattice representation of the direct shear test. a) deformations at the end of the simulation for 200 kPa. b) Evolution of deformation and lateral force.

$$\tau = \sigma_N \tan\phi_{fric} + c \tag{8}$$

where ϕ_{fric} represents friction angle and c represents apparent cohesion. The term cohesion is labelled as apparent because in reality granular materials exhibit non-cohesive behaviour (no shear resistance under no normal stress) [51]; this cohesive parcel of the shear resistance (c) is a result of the asymptotic linearization of the dependency of τ on σ_N. This approximation is assumed valid for the remainder of this work because, in the context of railway tracks, ballast is constrained longitudinally, resulting in longitudinal normal stresses.

In the lattice model, the frictional part of the resistance can be easily accommodated by making the shear connection of the stick-slip type, in series with the “compaction” spring defined in the previous section, and such that the slip force is given as a function of the normal force (Figure 7a):

$$F_{shear,max} = -F_{shear,min} = (F_1 + F_2 + F_3)\tan\phi_{fric} \tag{9}$$

The cohesive part can, in turn, be accommodated in the diagonal connection by making these connections also of the stick-slip type (Figure 7b) and such that the sliding force is given by

$$F_{diag,max} = -F_{diag,min} = W\frac{d}{\sqrt{2}}c \tag{10}$$

where d is the diameter of the lattice particle, W is the dimension in the out-of-plane direction, and c the cohesion.

The dimensions of the boxes used in the reference tests [50] are: for the top box, height = 0.3 m, length = 0.6 m, and width = 0.6 m (out-of-plane direction); for the lower box, height = 0.25 m, length = 0.7 m, and width = 0.6 m. Different ballast samples were submitted to vertical forces (on the top box) equivalent to a normal stress of 50, 100 and 200 kPa, and for each applied force, the lower box was moved laterally until failure. For the “fresh” ballast case (considered here as reference; “fresh” is how authors labelled the ballast sample that was tested for the first time, without reusage of particles) the following values for the friction angle and for the apparent cohesion were observed: $\phi_{fric} = 60.27°$, $c = 9950$ Pa. These tests are reproduced next with the lattice and the non-linear connections defined in this and previous sections. For the simulation, the lengths of the upper and lower boxes are assumed the same (0.6 m), and from the particle size distribution described in the reference work, a characteristic particle size of 0.03m is chosen. Figure 8a shows the lattice model and the boundary conditions (corresponding to a shear strain of 0.1 and for the 200 kPa load case).

It is assumed that the compaction properties of the ballast sample used in the direct shear test are the same as the sample used in the cyclic test of the previous section. Hence, the properties of the normal connections of the lattice are the same as in Subsection 2.3, with a few adjustments to account for the different geometrical dimensions. The following expressions are used to scale a lattice from dimensions 1 to dimensions 2 (diameter d and out of plane dimension W) while keeping the same mechanical properties (overall stiffness and resistance):

$$\begin{array}{ll} \text{Stiffness related parameters :} & k^2 = k^1 W^2 / W^1 \\ \text{Force related parameters :} & F^2 = F^1 \left(d^2 W^2\right) / \left(d^1 W^1\right) \\ \text{Displacement related parameters(gap and } r_{max}) : & u^2 = u^1 d^2 / d^1 \end{array} \tag{11}$$

The maximum forces for the shear and diagonal connection are given from Eqs. (9) and (10), respectively. Figure 8b shows the obtained deformation vs lateral force, and compares with those observed in the reference tests.

As observed in Figure 8b the force-displacement relationship is not captured very well. Fine-tuning the different model parameters

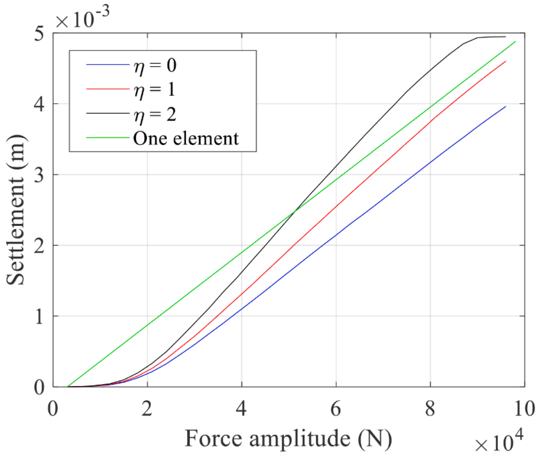

Figure 9. Maximum settlement as function of load amplitude for different correction factors η.

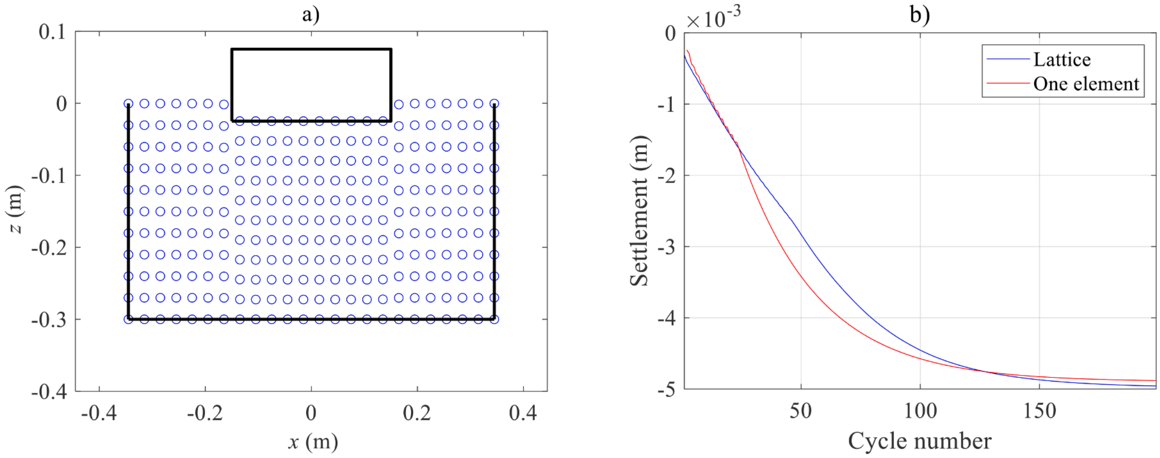

Figure 10. Response of the lattice due to the cyclic load. a) residual deformations at the end of the last load cycle (deformation is multiplied by 5 for visual purposes). b) Evolution of settlement at the end of each cycle (position of sleeper under the minimum load of 5 kN).

will not lead to better matches in all the three scenarios, since they show a shear stiffness that is dependent on the normal stress. The different stiffnesses may be related to interlocking of ballast particles and other non-linear geometric effects that cannot be reproduced with this lattice type. However, the shear strength is reproduced reasonably well, and for the purpose of the lattice model, which aims at capturing the global behaviour of ballast, that is considered good enough. Nevertheless, a possibility to obtain better matches between simulation and direct shear tests is to make the shear stiffness k_{shear} dependent on the load F carried by the compression spring; on the negative side, this will lead to more complicated solution procedures.

3.1. Cyclic loading of ballast simulated with a lattice including shear failure

The cyclic test of Section 2 is simulated again, this time with the shear and diagonal connections made non-linear as described in the beginning of this section. The values assumed for the friction angles and apparent cohesion are those reported in the direct shear tests, i.e., $\phi_{\mathrm{fric}} = 60.27^\circ$ and $c = 9950$ Pa. It is important to note that, in the case of a lattice, the applied vertical force is no longer counteracted solely by the vertical springs; part of that force is resisted by the diagonal springs up to their maximum force (related to cohesion). This means that in order to obtain the maximum residual deformation $r_{\max}$ under the same applied force F_{ref}, the reference force of the lattice connections $F^{\mathrm{lat}}_{\mathrm{ref}}$ must be corrected to account for the fact that the vertical connections will carry less force. The total vertical component of the cohesive force at the vertical surfaces passing through the edges of the sleeper is $F_{\mathrm{cohesion}} = 2cWh$ (where h is the height of the ballast layer); based on that, it is reasonable to take the corrected value of $F^{\mathrm{lat}}_{\mathrm{ref}}$ as

$$F^{\mathrm{lat}}_{\mathrm{ref}} = \frac{F_{\mathrm{ref}} - 2cWh\eta}{N^{\mathrm{load}}_{x}}, \tag{12}$$

where η is a correction factor. Figure 9 shows the maximum obtained settlement (after many cycles) for different load amplitudes and for $\eta = 0$, $\eta = 1$ and $\eta = 2$, and compares them with the expected settlement as obtained when using only one element (green line; this line is straight, as imposed by Eqs. (4)-(5)). If $\eta = 0$ (blue line), no correction is applied and under the load F_{ref} the maximum settlement is smaller than $r_{\max}$; if $\eta = 1$ (red line), the maximum settlement is attained for the force amplitude F_{ref}; if $\eta > 1$ (black line), the maximum settlement is reached for force amplitudes lower than F_{ref}. The deviation from the settlement expected with a single vertical non-linear element (green line) is more balanced for $\eta = 2$ (smaller at some parts and larger at others) than for $\eta = 1$ (always smaller), and therefore for the remainder of this work the correction factor $\eta = 2$ is used. Note that for different ballast samples, for which different lattice parameters are defined, the curves shown in Figure 8 may be different; it is therefore important to calculate these lines for the lattice parameters to be considered, and then chose the value of η that is believed to better describe the dependence of the maximum settlement on the applied force amplitude.

The results from the simulation of the cyclic test, considering shear failure and the corrected $F_{\text{ref}}^{\text{lat}}$ are represented in Figure 10. It is clear that the introduction of sliding in the shear and diagonal connections allows the lattice to settle as expected, and although there are deviations compared to the simulation with only one element, the ultimate settlement is very similar (as imposed) and the settlement evolution follows the same trend. The examination of Figure 10a reveals that most of the resistance to the vertical motion is offered by the particles below the sleeper, whilst the particles to the left and right of the sleeper remain almost in place, suggesting that the shear and diagonal connections at the edges of the sleeper reach sliding (shear failure). That is not the case in Figure 6a.

An overview of the tuning procedure presented in Sections 2 and 3 is given in Appendix A.

4. Solution method for the dynamic equations

The examples shown in Sections 2 and 3 were solved considering quasi-static conditions, i.e., assuming that each load cycle was slow enough that the inertial forces were insignificant. The loading and unloading of sleepers due to train passages happen at a faster rate that may lead to wave generation and propagation, meaning that statics may no longer be a valid assumption. Hence, it is important to consider the mass of the particles and the corresponding inertial forces.

The motion of the lattice masses is given by the second Newton's law

$$\mathbf{M}\ddot{\mathbf{u}} = \mathbf{f}_{\text{ext}} + \mathbf{f}_{\text{int}}(\dot{\mathbf{u}}, \mathbf{u}) \tag{13}$$

where $\mathbf{M}$ is a diagonal matrix containing the masses of the particles, $\mathbf{u}$ is a vector containing the motion of each particle (horizontal and vertical), $\mathbf{f}_{\text{ext}}$ is a vector containing the externally applied forces, and $\mathbf{f}_{\text{int}}(\dot{\mathbf{u}}, \mathbf{u})$ is a vector containing the forces on each lattice mass that result from the deformation of the lattice connections (the non-linearities are included in this vector); dots denote time derivatives. Eq. (13) can be solved with explicit methods like the Runge-Kutta, or implicit methods like the Newmark method. The first type of methods are quite easy to implement, but need very small time steps for them not to diverge. On the other hand, implicit methods have less stability issues and can work with larger time steps, but they require the solution of a system of non-linear equations at each time step. The method employed in this work falls in the category of implicit methods, but with some simplifications in order to make it faster and more attractive for large simulations. The derivation of the method starts with expanding the non-linear term $\mathbf{f}_{\text{int}}(\dot{\mathbf{u}}, \mathbf{u})$ in a first order Taylor series approximation around the generic state $\dot{\mathbf{u}}^*, \mathbf{u}^*$

$$\mathbf{f}_{\text{int}}(\dot{\mathbf{u}}, \mathbf{u}) \approx \mathbf{f}_{\text{int}}(\dot{\mathbf{u}}^*, \mathbf{u}^*) - \mathbf{K}(\dot{\mathbf{u}}^*, \mathbf{u}^*)(\mathbf{u} - \mathbf{u}^*) - \mathbf{C}(\dot{\mathbf{u}}^*, \mathbf{u}^*)(\dot{\mathbf{u}} - \dot{\mathbf{u}}^*) \tag{14}$$

where the stiffness matrix

$$\mathbf{K}(\dot{\mathbf{u}}^*, \mathbf{u}^*) = -\left.\frac{\partial \mathbf{f}_{\text{int}}(\dot{\mathbf{u}}, \mathbf{u})}{\partial \mathbf{u}}\right|_{(\dot{\mathbf{u}}^*, \mathbf{u}^*)} \tag{15}$$

and the damping matrix

$$\mathbf{C}(\dot{\mathbf{u}}^*, \mathbf{u}^*) = -\left.\frac{\partial \mathbf{f}_{\text{int}}(\dot{\mathbf{u}}, \mathbf{u})}{\partial \dot{\mathbf{u}}}\right|_{(\dot{\mathbf{u}}^*, \mathbf{u}^*)} \tag{16}$$

assemble all the springs and damper components of the lattice that are active (not sliding / gap filled) for the state $\dot{\mathbf{u}}^*, \mathbf{u}^*$. After replacing the Taylor expansion in Eq. (13), the system of equations of motion of the lattice particles becomes

$$\mathbf{M}\ddot{\mathbf{u}} + \mathbf{C}(\dot{\mathbf{u}}^*, \mathbf{u}^*)(\dot{\mathbf{u}} - \dot{\mathbf{u}}^*) + \mathbf{K}(\dot{\mathbf{u}}^*, \mathbf{u}^*)(\mathbf{u} - \mathbf{u}^*) = \mathbf{f}_{\text{ext}} + \mathbf{f}_{\text{int}}(\dot{\mathbf{u}}^*, \mathbf{u}^*) \tag{17}$$

For time discretization the Newmark method is applied [52]. This method defines rules for the evolution of accelerations, velocities and displacements within a time step through the equations

$$\begin{aligned} \dot{\mathbf{u}}^j &= a_1\left(\mathbf{u}^j - \mathbf{u}^{j-1}\right) - a_4\dot{\mathbf{u}}^{j-1} - a_5\ddot{\mathbf{u}}^{j-1} \\ \ddot{\mathbf{u}}^j &= a_0\left(\mathbf{u}^j - \mathbf{u}^{j-1}\right) - a_2\dot{\mathbf{u}}^{j-1} - a_3\ddot{\mathbf{u}}^{j-1} \end{aligned} \tag{18}$$

where the superscript j refers to the time instant $t = j\Delta t$, and the constants a_0 to a_5 are given by [53]

$$\begin{aligned} &a_0 = \frac{1}{\beta\Delta t^2}, \quad a_1 = \frac{\gamma}{\beta\Delta t}, \quad a_2 = \frac{1}{\beta\Delta t} \\ &a_3 = \frac{1}{2\beta} - 1, \quad a_4 = \frac{\gamma}{\beta} - 1, \quad a_5 = \Delta t\left(\frac{\gamma}{2\beta} - 1\right) \end{aligned} \tag{19}$$

The constants β and γ are the Newmark parameters, and are set at $\beta = 0.25$ and $\gamma = 0.5$, which leads to unconditionally stable solvers, at least in the case of linear systems. After replacing in Eq. (17) $\ddot{\mathbf{u}}$, $\dot{\mathbf{u}}$ and $\mathbf{u}$ by $\ddot{\mathbf{u}}^j$, $\dot{\mathbf{u}}^j$ and $\mathbf{u}^j$, and making use of the relations in Eq. (18), the discrete equations of motion become

$$\begin{aligned} a_0\mathbf{M}\mathbf{u}^j + a_1\mathbf{C}(\dot{\mathbf{u}}^*, \mathbf{u}^*)\mathbf{u}^j + \mathbf{K}(\dot{\mathbf{u}}^*, \mathbf{u}^*)\mathbf{u}^j \quad = \quad & \mathbf{f}_{\text{ext}} + \mathbf{f}_{\text{int}}(\dot{\mathbf{u}}^*, \mathbf{u}^*) \\ & + \mathbf{M}\left(a_0\mathbf{u}^{j-1} + a_2\dot{\mathbf{u}}^{j-1} + a_3\ddot{\mathbf{u}}^{j-1}\right) \\ & + \mathbf{C}(\dot{\mathbf{u}}^*, \mathbf{u}^*)\left(a_1\mathbf{u}^{j-1} + a_4\dot{\mathbf{u}}^{j-1} + a_5\ddot{\mathbf{u}}^{j-1} + \dot{\mathbf{u}}^*\right) \\ & + \mathbf{K}(\dot{\mathbf{u}}^*, \mathbf{u}^*)\mathbf{u}^* \end{aligned} \tag{20}$$

For the equations of motion to be solved in an absolute implicit fashion, then the state $\dot{\mathbf{u}}^*, \mathbf{u}^*$ must correspond to the state at the time step $t = j\Delta t$, i.e., $\dot{\mathbf{u}}^* = \dot{\mathbf{u}}^j$ and $\mathbf{u}^* = \mathbf{u}^j$. This leads to Eq. (20) becoming a system of non-linear equations that must be solved iteratively, for example, with the Newton-Raphson method (eventually with the arc-length strategy to help in convergence). Application of this method leads to the following iterative scheme:

$$\begin{aligned} &\mathbf{u}^{j,0} = \mathbf{u}^{j-1} \\ &\dot{\mathbf{u}}^{j,0} = \dot{\mathbf{u}}^{j-1} \\ &\text{for } i = 1 \text{ until convergence} \\ &\left\{ \begin{aligned} &\left(a_0\mathbf{M} + a_1\mathbf{C}\left(\dot{\mathbf{u}}^{j,i-1}, \mathbf{u}^{j,i-1}\right) + \mathbf{K}\left(\dot{\mathbf{u}}^{j,i-1}, \mathbf{u}^{j,i-1}\right)\right)\mathbf{u} = \mathbf{f}_{\text{ext}} + \mathbf{f}_{\text{int}}\left(\dot{\mathbf{u}}^{j,i-1}, \mathbf{u}^{j,i-1}\right) \\ &\qquad + \mathbf{M}\left(a_0\mathbf{u}^{j-1} + a_2\dot{\mathbf{u}}^{j-1} + a_3\ddot{\mathbf{u}}^{j-1}\right) \\ &\qquad + \mathbf{C}\left(\dot{\mathbf{u}}^{j,i-1}, \mathbf{u}^{j,i-1}\right)\left(a_1\mathbf{u}^{j-1} + a_4\dot{\mathbf{u}}^{j-1} + a_5\ddot{\mathbf{u}}^{j-1} + \dot{\mathbf{u}}^{j,i-1}\right) \\ &\qquad + \mathbf{K}\left(\dot{\mathbf{u}}^{j,i-1}, \mathbf{u}^{j,i-1}\right)\mathbf{u}^{j,i-1} \\ &\Delta\mathbf{u} = \mathbf{u} - \mathbf{u}^{j,i-1} \\ &\mathit{if} \parallel \Delta\mathbf{u} \parallel > \mathit{arc} \rightarrow \Delta\mathbf{u} = \frac{\Delta\mathbf{u}}{\parallel \Delta\mathbf{u} \parallel}\mathit{arc} \\ &\mathbf{u}^{j,i} = \mathbf{u}^{j,i-1} + \Delta\mathbf{u} \\ &\dot{\mathbf{u}}^{j,i} = a_0\left(\mathbf{u}^{j,i} - \mathbf{u}^{j-1}\right) - a_2\dot{\mathbf{u}}^{j-1} - a_3\ddot{\mathbf{u}}^{j-1} \end{aligned} \right. \end{aligned} \tag{21}$$

Because this iterative scheme demands the re-assemblage of the stiffness and damping matrices and a solution of a system of linear equations every iteration of each time step, it becomes quite unattractive for large domains, mostly because of the time burden. To go around that, it can be assumed that within one time interval the variations in the non-linearities are small, and in this way linearize the system of equations about the state of the previous time step, i.e., $\dot{\mathbf{u}}^* = \dot{\mathbf{u}}^{j-1}$ and $\mathbf{u}^* = \mathbf{u}^{j-1}$. This semi-implicit-semi-explicit approach corresponds to one iteration of scheme (21) (without arc-length) and leads to the following system of equations to be solved every time-step:

$$\begin{aligned} \left(a_0\mathbf{M} + a_1\mathbf{C}\left(\dot{\mathbf{u}}^{j-1}, \mathbf{u}^{j-1}\right) + \mathbf{K}\left(\dot{\mathbf{u}}^{j-1}, \mathbf{u}^{j-1}\right)\right)\mathbf{u}^j = \mathbf{f}_{\text{ext}} + \mathbf{f}_{\text{int}}\left(\dot{\mathbf{u}}^{j-1}, \mathbf{u}^{j-1}\right) & \\ + \mathbf{M}\left(a_0\mathbf{u}^{j-1} + a_2\dot{\mathbf{u}}^{j-1} + a_3\ddot{\mathbf{u}}^{j-1}\right) & \\ + \mathbf{C}\left(\dot{\mathbf{u}}^{j-1}, \mathbf{u}^{j-1}\right)\left(a_1\mathbf{u}^{j-1} + a_4\dot{\mathbf{u}}^{j-1} + a_5\ddot{\mathbf{u}}^{j-1} + \dot{\mathbf{u}}^{j-1}\right) & \\ + \mathbf{K}\left(\dot{\mathbf{u}}^{j-1}, \mathbf{u}^{j-1}\right)\mathbf{u}^{j-1} & \end{aligned} \tag{22}$$

Even though the semi-implicit-semi-explicit approach is more appealing than the implicit one, it still requires the assemblage of the stiffness and damping matrices at each time step. If these matrices were to remain constant throughout the simulation, then solving the system of equations could be made more efficient, since the system matrix could be factorized at the beginning of the simulation and then reused every time step. With this in mind, Eq. (22) is approximated to

$$\begin{aligned} \left(a_0\mathbf{M} + a_1\mathbf{C}^0 + \mathbf{K}^0\right)\mathbf{u}^j \quad = \quad & \mathbf{f}_{\text{ext}} + \mathbf{f}_{\text{int}}\left(\dot{\mathbf{u}}^{j-1}, \mathbf{u}^{j-1}\right) \\ & + \mathbf{M}\left(a_0\mathbf{u}^{j-1} + a_2\dot{\mathbf{u}}^{j-1} + a_3\ddot{\mathbf{u}}^{j-1}\right) \\ & + \mathbf{C}^0\left(a_1\mathbf{u}^{j-1} + a_4\dot{\mathbf{u}}^{j-1} + a_5\ddot{\mathbf{u}}^{j-1} + \dot{\mathbf{u}}^{j-1}\right) \\ & + \mathbf{K}^0\mathbf{u}^{j-1} \end{aligned} \tag{23}$$

where the matrices $\mathbf{K}^0 = \mathbf{K}(\mathbf{u}^0, \dot{\mathbf{u}}^0)$ and $\mathbf{C}^0 = \mathbf{C}(\mathbf{u}^0, \dot{\mathbf{u}}^0)$ are the stiffness and damping matrices for the initial state system (if $\mathbf{u}^0 = \mathbf{0}, \dot{\mathbf{u}}^0 =$

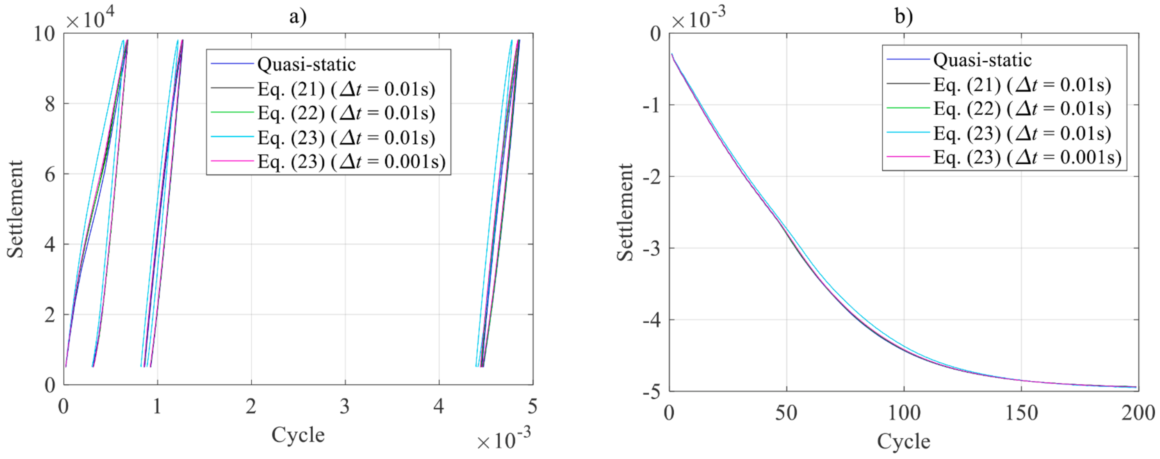

Figure 11. Dynamic response of the lattice. a) loading and unloading behaviour for first, 10th and 100th load cycles. b) evolution of settlement at the end of each cycle (position of sleeper under the minimum load of 5 kN). All lines are virtually the same, except for the cyan one.

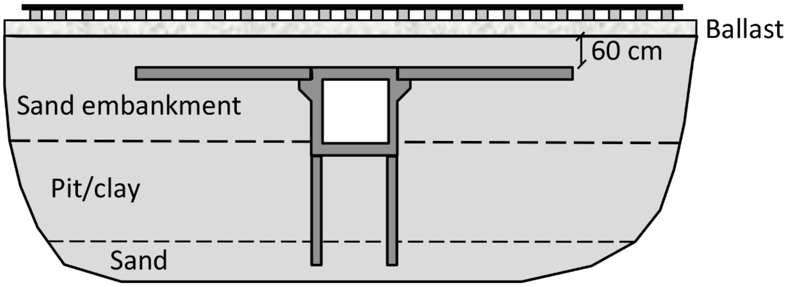

Figure 12. Culvert going under a railway line [44].

0, then the initial state is undeformed). Using Eq. (23) is equivalent to assuming that the system behaves linearly, and correcting for that by adding the force vector $\mathbf{f}_{\text{int}}(\dot{\mathbf{u}}^{j-1}, \mathbf{u}^{j-1}) + \mathbf{C}^0\dot{\mathbf{u}}^{j-1} + \mathbf{K}^0\mathbf{u}^{j-1}$, which corresponds to the difference between linearized forces and non-linear forces at the previous state.

Next, the cyclic test described in Sections 2 and 3 is simulated by using Eqs. (21)-(23) and the results are compared with the quasi-static results. The loading frequency is 3 Hz, the same as in the lab test, and the density of ballast is assumed $\rho = 1800$ kg/m^3, which leads to a particle mass of $m^{\text{lat}} = \rho d^2 W = 4.05$ kg (which may seem a large value, but it corresponds to a fictitious condensed mass of all ballast particles within a given area or volume). Some viscous damping is assumed in the shape of dashpots of the type $C^{\text{lat}}_{\text{normal}} = 0.001(k^{\text{lat}}_1 + k^{\text{lat}}_2)$ for the normal connections, $C^{\text{lat}}_{\text{shear}} = 0.001k^{\text{lat}}_{\text{shear}}$ for the shear connections and $C^{\text{lat}}_{\text{diag}} = 0.001k^{\text{lat}}_{\text{diag}}$ for the diagonal connections; the dashpots are assumed to be linear, i.e., in the event of sliding or loss of contact, the dampers are still active. A time step of $\Delta t = 0.01$ s is used for the dynamic simulations (for the simulation using Eq. (23), an extra simulation with time $\Delta t = 0.001$ s step is performed). Figure 11a compares force-displacement evolution of the sleeper for the first, 10th and 100th load cycles for the different scenarios, and Figure 11b shows the evolution of the settlement with the number of load cycles.

It is clear from Figure 11 that using Eq. (23) with the time step $\Delta t = 0.01$ s (cyan lines) leads to small differences of the response, when compared to the other scenarios. That difference can be reduced to almost zero by reducing the time step to $\Delta t = 0.001$ s (magenta), in which case the response is virtually the same as those obtained with Eqs. (21) and (22) (black and green lines). The fact that these lines are not distinguishable means that within one time step no major non-linearities occur. When compared to the quasi-static results, the dynamic simulations lead also to virtually the same results (both in terms of load-unload behaviour, Figure 11a, as in terms of settlement evolution, Figure 11b), meaning that the loading frequency (3 Hz) does not excite the ballast sample dynamically, at least not for the considered boundary conditions. However, for the railway case, the loading and unloading during a train passage happens at higher frequencies (a train travelling at 60 m/s and whose axles of the same bogie are 3 m apart induce a fundamental frequency of 20 Hz), and the lower boundary is flexible (unlike in the experiments, where it is rigid), and thus differences between quasi-static and dynamic simulations are more likely to occur. Hence, despite the fact that in this case a good correspondence between quasi-static and dynamic simulations is observed, for studying ballast settlement due to train passages quasi-static analyses may not suffice. Also observable in Figure 11a is the stiffening of the ballast with the number of load cycles, a feature that is imposed by the gap spring.

5. Application to a railway track

5.1. Culvert passaging underneath the track

In this section, the non-linear connections are used to estimate how settlement of ballast develops in a railway track. The focus is put on differential settlement in zones with foundation-stiffness variations, and for that matter the scenario of a culvert passing underneath a railway track is taken as reference. The considered scenario is based on a stretch of the Dutch railway line, which is thoroughly described by other authors [49,54,55], and has been simulated using a linear lattice in a previous work [44]. In the present work, the same scenario is simulated but using a non-linear lattice representing ballast. A sketch of the problem to be modelled is shown in Figure 12 (taken from [3]); the culvert spans 4 sleeper bays, and the approach slabs (0.3 m of thickness) span 7 sleeper bays on each side of the culvert. The track is to be subjected to multiple train passages, and the evolution of differential settlement is analysed.

The solution strategy is the same as described in [44]. The domain is divided into three regions: a left region that is linear, periodic and semi-infinite, and is treated semi-analytically; a mid-region that represents the zone of stiffness variations and where non-linear behaviour of ballast is allowed; a right region, which, like the left region, is semi-infinite and treated semi-analytically. In order to incorporate the non-linearities in the mid-region, the system of Eqs. (11) in reference [44], which describes the time-stepping procedure for the three-region model, must be augmented/adjusted with the non-linear components expressed in Eq. (23), i.e., for the non-linear connections, the stiffness and damping matrices must correspond to the matrices $\mathbf{K}^0$ and $\mathbf{C}^0$ at the beginning of each simulation/train passage, and the right-hand-side must now include the difference between linearized internal forces and non-linear internal forces: $\mathbf{f}_{\text{int}}(\dot{\mathbf{u}}^{j-1}, \mathbf{u}^{j-1}) + \mathbf{C}^0\dot{\mathbf{u}}^{j-1} + \mathbf{K}^0\mathbf{u}^{j-1}$. At the end of each simulation/train passage, the system is solved statically, from which the starting state ($\mathbf{K}^0$ and $\mathbf{C}^0$) for the next passage is found. The weights of the rail and sleepers are considered as external forces throughout the simulations.

In total, 80 sleeper bays are modelled in the middle region, with the culvert centred in the middle. This number of sleeper bays was chosen such that there is enough distance on each side of the culvert/approach slabs so that they do not sense any boundary artefact. The boundary artefacts are not a result of the truncation of the mid-region and transient dynamic effects due to entrance or exit of the wheelsets (in practice, the three-region model is infinite so that does not occur); instead they are a consequence of the side regions responding linearly, not allowing any settlements, which is in contrast with the mid-region. The modelling and properties of each component are as follows:

- rails are modelled with a Euler-Bernoulli beam, with bending stiffness $EI_{\text{rail}} = 12.05 \times 10^6 \text{Nm}^2$ and unit mass $m_{\text{rail}} = 120$ kg /m (two UIC60 rails); rails are assumed perfectly levelled at the beginning of the first train passage;
- sleepers are modelled as rigid masses with inertia $M_s = 315$ kg and rotation inertia $J_s = 4.73$ kgm^2; the centre-to-centre distance between sleepers is 0.6 m, and the bottom width of the sleepers is 0.3 m;
- rail pads are modelled with vertical and rotation springs and dampers, whose coefficients are $K_v = 10^8$ N /m, $C_v = 10^5$Ns /m, $K_\theta = 2.14 \times 10^5$ Nm and $C_\theta = 2.14 \times 10^2$Nms;
- under-sleeper pads are modelled with vertical springs and dampers, whose coefficients are $K_{\text{usp}} = 1.72 \times 10^8$ N /m and $C_{\text{usp}} = 1.72 \times 10^5$ Ns /m; these values are to be equally distributed over each ballast particle in contact with the sleeper; the ballast particle diameter is 0.03 m, so there are 11 particles in contact with each sleeper and 9 particles in between sleepers; also, in the mid-region, the rail pads are assumed to work only under compression;
- ballast is modelled as a linear lattice (as shown in Figure 1) in the side regions and in the first two and last two sleeper bays of the mid-region, and as a non-linear lattice in the remaining sleeper bays of the mid-region; the characteristic distance is $d = 0.03$ m; the linear properties are presented in Table 2 (Appendix B); the non-linear properties are the same described in Section 3, i.e., $k_1^{\text{lat}} = 90 \times 10^6$N /m, $k_2^{\text{lat}} = 30 \times 10^6$N /m, $k_3^{\text{lat}} = 60 \times 10^6$N /m, $F_{2,\text{max}}^{1,\text{lat}} = 75$ N, $F_{\text{ref}}^{\text{lat}} = 6825$ N, $g_3^{\text{lat}} = 0.041 \times 10^{-3}$ m, $r_{\text{max}}^{\text{lat}} = 0.73 \times 10^{-3}$ m (unlike in Sections 2 and 3, here it is considered the total settlement as observed in the cyclic loading of sleepers – 7.3 mm [13], and not the value offset by the settlement after the first load cycle), $\phi_{\text{fric}} = 60.27^\circ$, and $c = 9950$ Pa; the degradation-rate factor β_i is assumed constant;
- soil is modelled also as a single layer of a linear lattice, with depth 1.2 m and characteristic distance $d = 0.03$ m, and with properties presented in Table 3 (Appendix B); horizontal and vertical springs and dashpots are added at the lower row of masses to simulate non-reflective boundary, and their properties are $k_h = 1665 \times 10^6$N /m, $c_h = 13.8 \times 10^3$Ns /m, $k_v = 1.77 \times 10^6$N /m and $c_v = 720$ Ns /m; the properties considered for soil are justified in a previous work [44], where the procedure to go from measured properties to 2D models is explained;
- the approach slabs are also modelled with a linear lattice, for which case the properties of undamped concrete are assumed and the values are presented in Table 3 (Appendix B); the approach slabs are hinged at the connection points with the culvert;
- the culvert is assumed rigid and immovable, so it is simulated simply by fixing the lattice masses at the position of the culvert.

The track model is subjected to multiple passages of a X2000 train travelling at the speed 60 m/s (approximately 220 km/h, close to the upper limit of the operational speed in the Netherlands) and simultaneously to the weight of sleepers and rails (these last components are considered in order to pre-load the under-sleeper pads). The X2000 train is modelled with 20 equivalent oscillators, each representing a wheelset (the relative position of wheelsets can be found in [56]). For simplicity, the coupling between wheelsets via bogies and car bodies is not considered. In this way, each oscillator is composed of a top mass representing one quarter of the car body

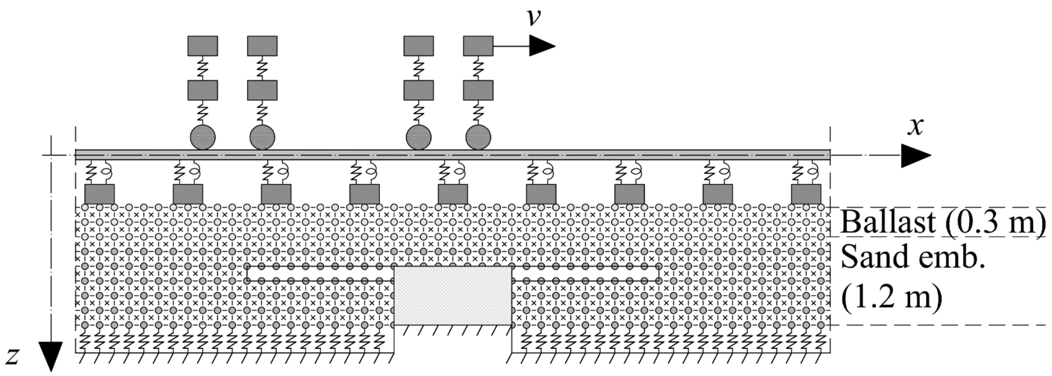

Figure 13. Schematics of the model: transition zone with a culvert and approach slabs; 1.2 m of the sand embankment is modelled explicitly through a lattice while the layers beneath (see Figure 12) are represented through equivalent springs-dashpots at the bottom. Note that the figure is not to scale (the lattice particles are much smaller than represented).

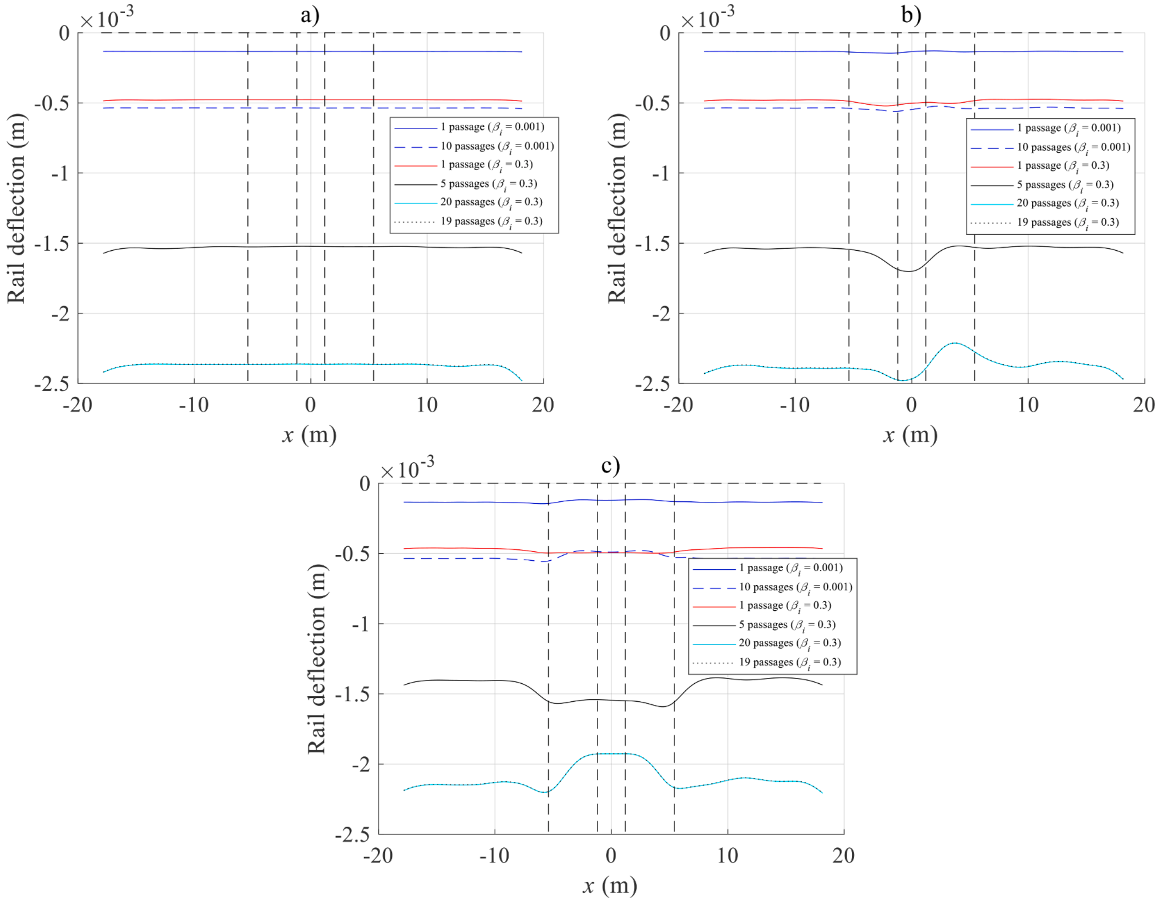

Figure 14. Rail position as number of train passages increases. a) uniform scenario; b) culvert scenario; c) culvert + approach slabs scenario.

(M_c = 8250 kg), a middle mass representing half of a bogie (M_b = 2500 kg) and a lower mass representing a wheelset (M_w = 1700 kg); masses M_c and M_b are connected via a spring-damper couple representing half of the secondary suspension system ($k_s = 656 \times 10^3$N/m, $c_s = 18 \times 10^3$Ns/m), and masses M_b and M_w are connected via a spring-damper couple representing the primary suspension system ($k_p = 3426 \times 10^3$N/m, $c_p = 36 \times 10^3$Ns/m); contact springs ($k_c = 2.4 \times 10^9$N/m) connect wheelsets and rails (this stiffness is made 100 times softer than it should, otherwise a very small time step would be required for convergence of the solver; in any case, tests with stiffer contact springs and smaller time steps revealed that the softer contact spring does not affect the results; the comparison is presented in Appendix C). The values of all parameters discussed here are also presented in a concise manner in Tables 1,

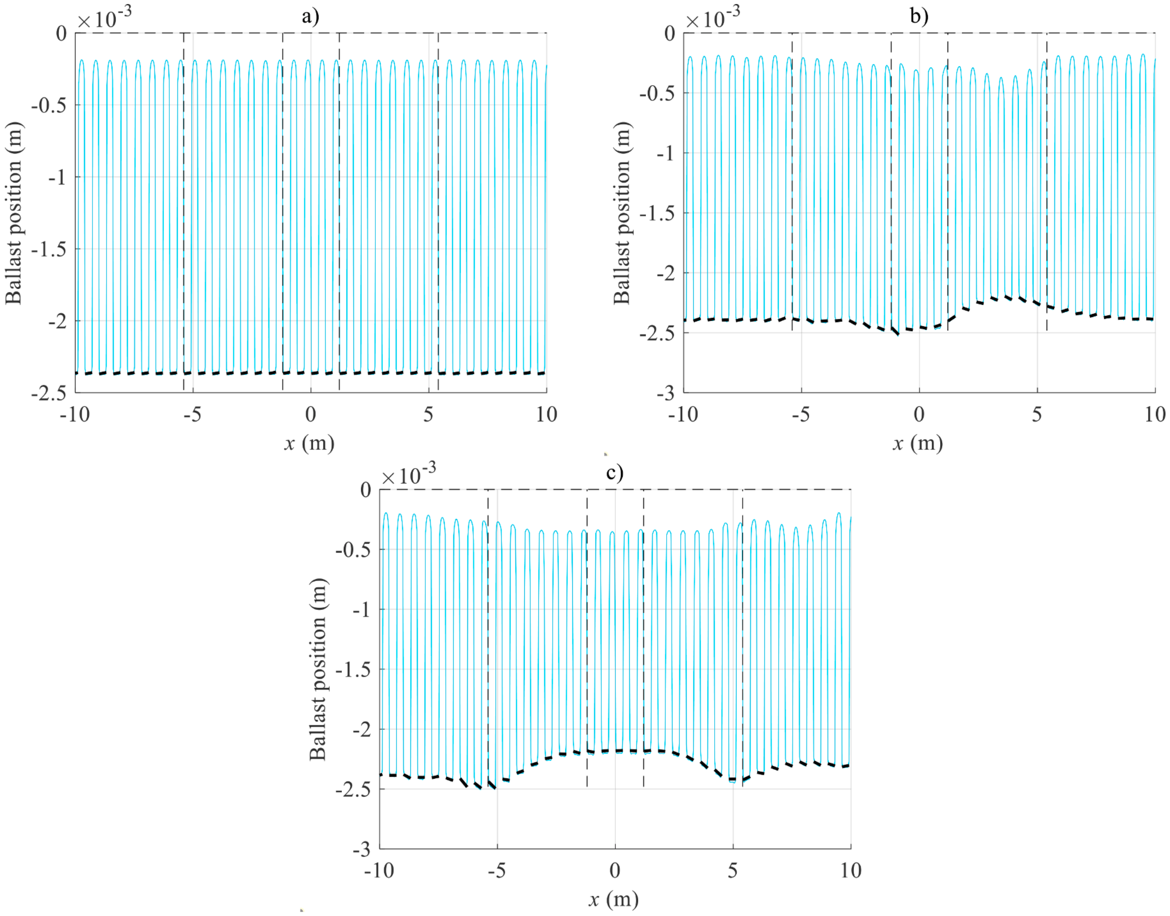

Figure 15. Position of surface of ballast (cyan) and sleepers (black) for stabilized deformation (after 20 passages with β_i=0.3). a) uniform scenario; b) culvert scenario; c) culvert + approach slabs scenario. Ballast shows troughs below the sleepers.

2, and 3, in Appendix B; unless specified otherwise, these values are used for all simulations in Section 5. Figure 13 presents a schematic of the model used in this section.

The incorporation of the oscillators in the time-stepping scheme requires further augmenting the system of Eqs. (11) (of work [44]) with the equations of motion of the oscillators plus the compatibility and equilibrium conditions. That task is trivial and does not demand extra explanations. However, in order to avoid a transient response of the vehicle at the transition between the settlement free and the settlement prone regions, which would be an artefact of the modelling approach, the oscillators are only active between the 10th and 70th sleeper bays of the mid-regions; outside these sleeper bays and in the side-regions, the wheelset are assumed to be moving loads with constant magnitude corresponding to the dead weight of all masses; for the train speed being considered, the dynamic component of the interaction forces at the uniform part of the track is less than 2% of the dead weight, so this assumption is valid.

5.2. Development of settlements

Three scenarios are considered next: the scenario in which no transition is present (uniform); a scenario in which only the culvert is present, but not the approach slabs (culvert); the scenario depicted in Figure 12, in which both approach slabs and culvert are present (culvert + approach slabs). For each scenario, the track is subjected to several passages of the X2000 train, and the development of residual deformations at the track is calculated. Two values of β_i are used: $\beta_i = 0.001$, which is more in line with the speed of compaction of ballast, as seen for the cyclic loading of sleepers in Section 2, and $\beta_i = 0.3$, which is artificial and leads to accelerated compaction, and therefore faster development of settlements. The motive for using $\beta_i = 0.3$ is that each simulation of a train passage takes a considerable amount of time, which makes it impractical to simulate tens of thousands of passages in order to obtain a stabilized differential settlement

Figure 14 shows the progressive position of the rail for the three scenarios (the black vertical lines represent the edges of approach slabs and culvert). For all three scenarios, it is seen that one passage of the train with $\beta_i = 0.001$ leads to residual deformations that are about one fifth of the deformations obtained with one passage with $\beta_i = 0.3$; in fact, 10 passages with $\beta_i = 0.001$ are needed to obtain residual deformations of the same order of magnitude as those of one passage with $\beta_i = 0.3$. For this reason, and because it is not

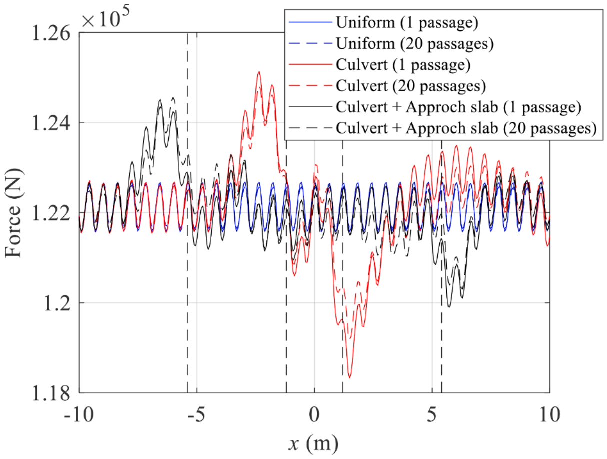

Figure 16. Wheel-rail contact force for the three scenarios.

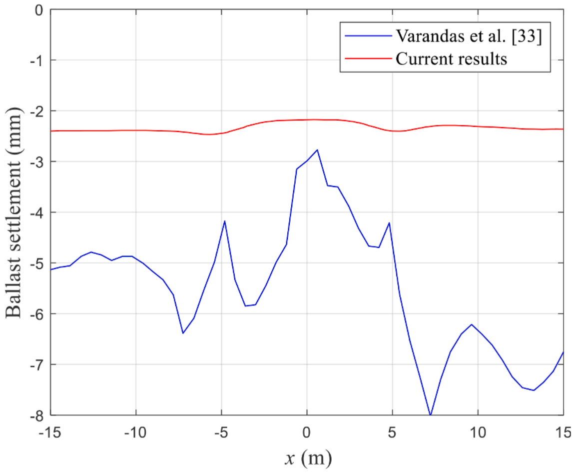

Figure 17. Ballast settlement under the sleepers in the transition zone; comparison of the current results and the ones obtained by Varandas et al. [33]

feasible (time wise) to reach a converged situation with $\beta_i = 0.001$, these results are not further analysed.

In all three scenarios, the deformation after 20 passages with $\beta_i = 0.3$ (cyan lines) have stabilized (the deformation after 19 passages overlaps the one after 20 passages in Figure 14). For the uniform scenario (Figure 14a), it is seen that the residual deformation of the rail does not change with the longitudinal position, which is to be expected since there is no heterogeneity justifying any difference in behaviour. There are nevertheless some small differences at the edges of the shown domain (observed in the three scenarios) which are caused by the boundary artefacts discussed in the previous subsection; these differences are not seen at the positions of culvert and approach slabs, indicating that the number of sleeper bays used in the simulations is enough. When only the culvert is used (Figure 14b), the deformations are larger at the location of the culvert than right next to it; the differential position of the rail reaches about one quarter of a millimetre. For the case of approach slabs + culvert (Figure 14c), the residual deformation is larger at the edges of the approach slab and open track than above the culvert; also in this case, the differential position of the rail is about 0.25 mm.

The differential settlement at the rail level are quite small and spread over large distances (0.25 mm in a couple of meters), so it is not expected that the wheel forces changed considerably from first passage to last one, nor that the cumulative settlement of ballast has led to hanging sleepers. This is indeed verified in Figure 15, which shows the stabilized positions (after 20 passages with $\beta_i = 0.3$) of ballast (its upper surface) and sleepers, and in Figure 16, which shows the wheel-rail contact force for the leading wheelset during the first and the 20th train passage. As can be seen in Figure 16, the solid lines (representing first passage) and dashed lines (representing 20th passage) do not reveal significant differences, which confirms the above stated. Also, the force amplification due to the stiffness variations is only around 2%, which partly explains the small differential ballast compaction due to the culvert and/or approach slabs. Since the simulations showed a converging process of ballast settlement, along with an only moderate increase in transmitted forces, it can be concluded that ballast compaction and settlement purely due to a stiffness change of track support structure is insufficient to explain progressive track degradation as observed at some stage in transition zones of this type (culvert passage with or without

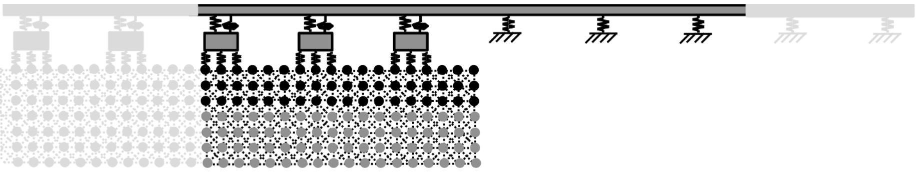

Figure 18. Model for ballast-lab transition. Side regions in lighter grey; mid-region in darker grey.

approach slabs). A similar conclusion was reached by other authors, using a different track model for the case of track-bridge interaction [37].

To give more perspective to the results obtained in this section, we compare them to the results obtained in literature that treat the same or similar transitions. Varandas et al. [33] modelled the same transition using a 1D model with an empiric settlement model for ballast. Their results have been compared to measurement data and showed a remarkable agreement (see Figure 12 in [33]).

Figure 17 presents a comparison of the results obtained by Varandas et al. [33] and the ones obtained in this paper. As it can be seen, these results differ significantly. However, the conditions simulated are essentially different; the authors of that study considered, unlike the current study, (i) accumulation of autonomous settlement of the subgrade (an imposed linearly-increasing settlement with time), (ii) hanging sleepers in the transition zone (leading to impact loading on the ballast), and (iii) an a-priori unlevel profile of the rail. These very different conditions can explain the larger differential settlement between different parts of the track caused by dynamic amplification of forces close to the culvert (they do report significantly higher amplification of forces than in the current work). It is important to emphasize that the current work studies the effect of the variation of railway track properties in longitudinal direction on ballast settlement by isolating it from all other settlement causes, while the scope of Ref. [33] is to reproduce field measurements. This explains the different choice of the features included in the model.

While the different conditions mentioned above can explain the difference in results close to the culvert, they cannot satisfactorily explain the considerably smaller settlement obtained in this work further away from the culvert (e.g., from around -15 m to -10 m), where the response does not exhibit dynamic amplification. This discrepancy in the settlement further away from the culvert is explained by how the settlement models in the two works are tuned. In this work, the lattice representing ballast is tuned to lab experiments that consider a ballast in good condition and of potentially different characteristics than the one at this specific transition zone; after the tuning process, none of the parameters are altered except for the degradation-rate coefficient β_i that does only affect the rate at which the settlement accumulates, and not the amount. The authors of [33] have tuned their empirical model partly based on lab experiments and partly to the data from the specific site to be simulated; while the values of their parameters α (expressing the dependence of the settlement on the loading amplitude); and β (controlling the progression of the settlement rate; similar to β_i in our model) were chosen from other experiments, the value of the parameter γ (the accumulated settlement with loading amplitude F_0 and number of cycles N_0; to some extent equivalent to $r_{\max}$ in our model) was tuned to match the field measurements. This led to values of γ much larger than in our case; for a load amplitude of 49 kN, the stabilized settlement in our case is around 2.4 mm (see Figure 5); in [33], for a reference load amplitude of 50 kN, values of γ have been chosen between 12.5 mm and 20 mm (outside the culvert zone; on the top of the culvert, the authors chose between 4.5 mm and 6 mm; see Table 4 in [33]). This fact explains very clearly the larger settlements obtained in [33] than in the current work. It also demonstrates the importance of tuning the lattice to lab experiments that employ the specific ballast composition encountered at the site of investigation.

Next, additional comparisons are made to two recent publications of the same authors of [33], namely Varandas et al. [36] and Paixão et al. [37]. In [36], a 3D FEM model is formulated for a track without a transition zone; for the ballast, a more advanced but similar empirical model (developed by Suiker and de Borst [35]) was used, which was tuned to lab experiments. The results predicted an accumulated settlement of the ballast under the sleeper of around 1.4 mm, a value which is much smaller than the one measured and predicted in [33], and more in line with the predictions made outside the transition zone in the current study. In [37], the same model as in [36] is used, but with a transition from open-track to a bridge. In this investigation, surprisingly, the ballast settlement was larger on the bridge (around 1.4 mm) compared to the zone adjacent to the bridge. The results from both studies support the qualitative and, to some extent, the quantitative results obtained in this study.

5.3. Ballast-slab transition

The previous example suggests that the ballast compaction mechanism on its own is insufficient to explain the occurrence of settlement of a progressive nature in the studied transition (culvert passage). However, hanging sleepers, which are attributed to a negative feedback loop, have not developed in the previous example. It is therefore of interest to investigate what happens in transitions where a train transits from a compaction-prone part of the track to a compaction-free part, a scenario in which hanging sleepers are likely to develop. This is the case, for example, in ballast-slab transitions, where ballast can settle, and the slab cannot (apart from autonomous settlement of the foundation [12], but that is not studied here). Therefore, in the following paragraphs, the transition from a ballasted track to a slab track is analysed. The ballasted part of the track is assumed the same as in the previous cases, and for the slab part it is assumed that the slab is rigid and immovable, and that only the rail nodes can move. The vertical stiffness and damping of the rail pads at the slab part are reduced to $K_{\mathrm{v}} = 1.9 \times 10^7 \mathrm{N/m}$ and $C_{\mathrm{v}} = 1.9 \times 10^4 \mathrm{Ns/m}$, which follows the common practice of trying to match the vertical stiffness of the two parts. An idealization of the model for this type of transition (based on the three-region strategy) is shown in Figure 18.

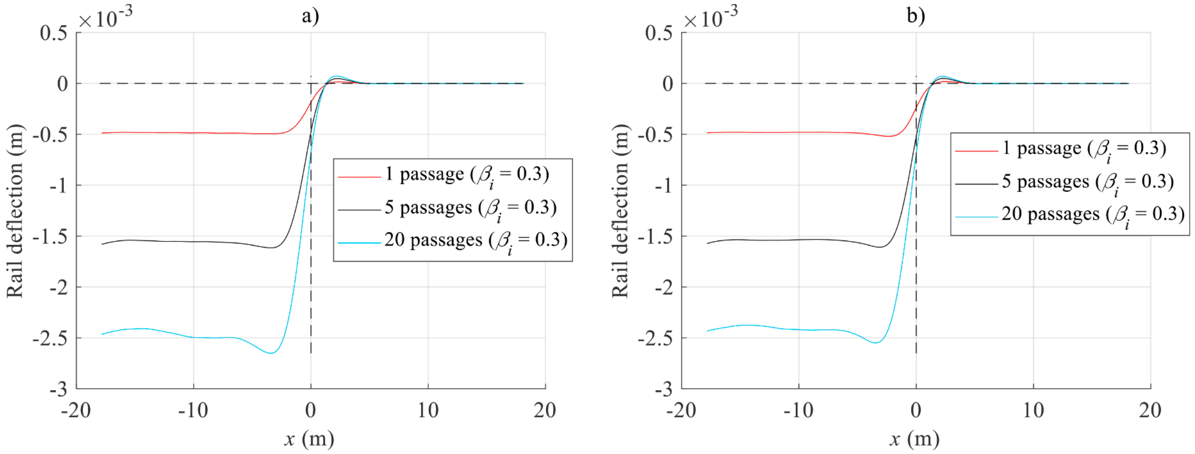

Figure 19. Rail position as number of train passages increases. a) slide scenario; b) bond scenario.

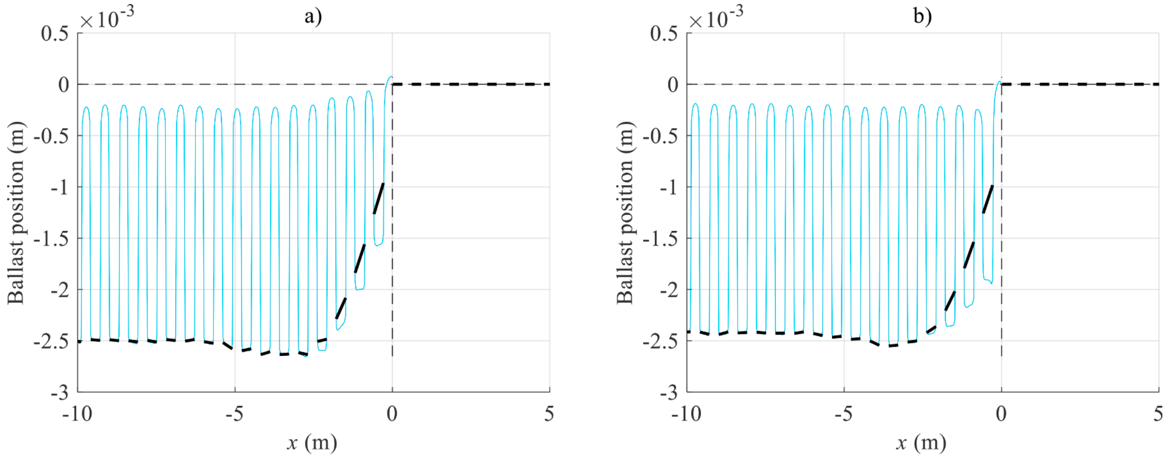

Figure 20. Position of surface of ballast (cyan) and sleepers (black) for stabilized deformation. a) slide scenario; b) bond scenario.

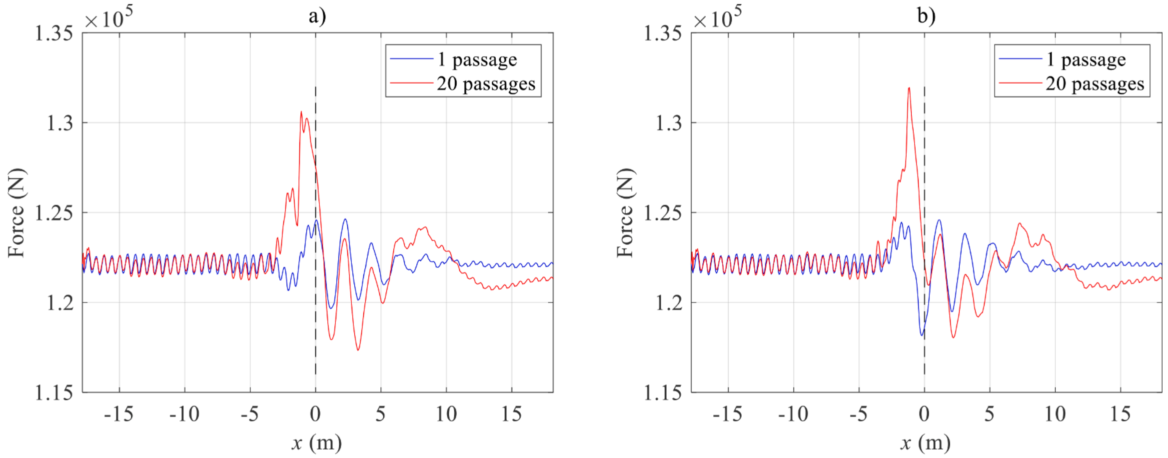

Figure 21. Evolution of wheel-rail contact force. a) slide scenario; b) bond scenario.

The boundary condition at the lattice-slab interface (right boundary of the lattice) is not well defined in the literature. Consequently, two limit cases are tested: the case in which the lattice particles at that interface can move freely in the vertical direction (slide), and the case in which the particles' vertical movement relative to the slab are prohibited (bond). In both cases, the horizontal motion is constrained. The real scenario is in between these two limit cases. A more realistic description would be through frictional sliding, in which a force resisting the vertical motion is applied based on the amplitude of the normal force, but the friction is unknown. For the two interface scenarios, the track is again subjected to multiple passages of the X2000 train at the speed of 60 m/s, and the evolution of the rail position, settlement of ballast, and wheel-rail forces are analysed. Figures 16-18 show these quantities.

The evolution of the position of the rail on the ballasted side of the track is very similar to that of the uniform scenario. On the contrary, on the ballastless part, because no settlement is allowed, the rail always returns to the same position. These two differing behaviours lead to an uneven rail profile at the interface, with a height difference of about 2.5 mm within a distance of about 4m (Figure 19). This is observed for both boundary conditions, showing that even though the dynamic behaviour at the interface may differ, that does not strongly affect the end terms of the settlement process.

It is further observed that the ballast settlement is almost constant until 5-6 sleeper bays before the transition, and close to the transition the ballast settlement decreases, but not completely to zero, as in the case of the rail. This leads to the occurrence of hanging sleepers, four in the case of the slide boundary condition (Figure 20a), and three in the case of bond boundary condition (Figure 20b). The sleeper left of the transition is where the gap is largest, reaching about 0.5 mm for the case of slide boundary condition and 1 mm for the case of the bond boundary condition. The gaps during the wheel passages are closed before the axle reaches the sleeper, and so strong impact loading does not occur; the force distribution is nevertheless changed, with the non-hanging sleepers bearing more force than the hanging ones, which explains the smaller ballast settlements under the hanging sleepers.

The larger differential position of the rail over a short distance leads to amplification of the wheel-rail forces. As seen in Figure 21, the increase in contact force of the leading wheelset at the interface during the first passage is solely 1.5% (compared to the average at the ballasted part of the track), but after the settlement has stabilized, the increase is 8-9%. These larger contact forces do not lead to further loss of vertical geometry of the track, but may partly explain other degradation indicators (e.g., accelerated wear of the rail and damage to sleepers) observed at these locations.

Overall, it is seen in this example that settlement of ballast can lead to hanging sleepers and increased contact forces. These features are not necessarily caused by variations in the stiffness as perceived by the oscillators (in this case, the stiffness of rail pads on the slab side are chosen to minimize these differences), but instead due to the junction of two types of tracks, one allowing settlement, and the other not. It is also observed that even though the differential settlements are more pronounced than in the previous example, the track profile still converges monotonously to a stabilized position. Therefore, in combination with the observations from the example of the culvert, these results suggest that ballast compaction as an independent mechanism is insufficient to explain cases of progressive degradation of the vertical geometry of the track in transition zones. Generally, the process must therefore involve other mechanisms such as differential autonomous/geotechnical settlement.

6. Concluding remarks

In this work, a non-linear lattice model that simulates the compaction behaviour of ballast material is presented, with the intention of studying the settlement behaviour of ballasted tracks in zones of stiffness variation. The non-linear properties of the lattice can be tuned to the results from lab tests (cyclic loading of ballast layers) and then be used for a wide variety of foundation conditions, since the tests only account for ballast. This versatility is one of the strongest points of the proposed model. To obtain accurate results, it is recommended that the lab tests employ the specific ballast composition encountered at the site of investigation. The model is able to capture phenomena like gradual settlement accumulation, the associated stiffening of the layer, and load dependent settlement. It is also seen that by making the degradation-rate factor of the model (β_i) cycle dependent, the evolution of settlements as observed during the lab tests can be reproduced almost exactly. However, such cycle dependency is expected to be highly dependent on the test conditions and on the history of the load amplitudes, so it is recommended that a constant value is used. In any case, at least for the studied examples, the final settlement profile of the layer does not depend on this parameter; β_i only affects how fast or slow the final configuration is achieved.

The use of the non-linear lattice model is exemplified by simulating the settlement accumulation due to successive train passages on tracks presenting distinct transition types: i) a zone with variations at the foundation, in which a culvert crosses under the track; ii) a transition from ballast track to slab track. In the first transition type, there are small differences in the settlement profiles over the culvert and approach slabs (when compared to the free part of the track), but these difference are insufficient to increase the wheel-rail contact forces or to lead to hanging sleepers. On the contrary, the ballast-slab transition scenario showed that as ballast compacts, the unlevelled rail leads to amplification of contact forces and to hanging sleepers. Nonetheless, the two scenarios showed that ballast compaction, on its own, is insufficient to explain occurrences of progressive deterioration of the vertical geometry of the track. Generally, other mechanisms such as differential geotechnical/autonomous settlement of the subgrade or mechanisms such as penetration of granular layers with different grain sizes due to particle migration across the interface, resulting in volumetric reduction of the track profile, must be taken into account in the initiation phase to explain such localised geometrical degradation processes.Eq. 14-16, 19

Declaration of Competing Interest

The authors declare that they have no known competing financial interests or personal relationships that could have appeared to influence the work reported in this paper.

Acknowledgments

The work published in this paper has been supported by the Dutch Technology Foundation TTW (Project 15968) – part of the Netherlands Organisation for Scientific Research (NWO), and by the Dutch infra manager ProRail. The latter grant is in the framework of a long term-research program aiming at an improved understanding of the physics of track degradation under train loading. The authors would also like to acknowledge the fruitful discussion with Akke Suiker from Eindhoven University of Technology regarding the proposed model.

Appendix A

In this appendix, we summarize the procedure of tuning the lattice representing ballast to lab experiments. The detailed explanations and assumptions made are presented in Sections 2 and 3. The aim of this summary is to present in a concise manner the tuning procedure to be used by possible users of this model and to give an overview for the reader.

1) Normal connection

a. Using one normal connection (Figure 2a), parameters g_3, k_1, k_2, k_3 and $F^1_{2,\max}$ are derived from lab experiments of ballast samples under cyclic loading. More specifically, these parameters can be determined from the first and last load-unload cycles measured in cyclic experiments. We recommend using $F^1_{2,\min} = 0$.

b. Next, $r_{\max}$ is defined from experiments observing the maximum settlement of the ballast sample. F_{ref} is the amplitude of the cyclic load that leads to $r_{\max}$.

c. Degradation-rate coefficient β_i is tuned such that the settlement accumulation rate is similar to the one in the experiments. The larger the β_i, the faster the damage accumulation. However, β_i can be manipulated depending on the scenario to be modelled. (For example, in the present work, hundreds of thousands of cycles with the whole railway track model cannot be simulated; therefore, because we are interested in the final settlement configuration, β_i is artificially increased to achieve the final configuration of the settlement after fewer cycles.)

d. All the other parameters necessary for the normal connection are obtained from the ones above using Eqs. (2), (3), (5) and (7).

e. The obtained parameters approximate the behaviour of a ballast sample by only one connection. Therefore, the obtained parameters need to be distributed over the lattice to be considered. The forces and stiffnesses are distributed over the number of particles in contact with the sleeper. $r_{\max}$ is distributed over the number of particles in z-direction; for example, for a ballast layer of 0.3 m and a nominal particles size of 0.03 m, there will be 10 connections; consequently, $r_{\max}$ obtained using one connection is divided by 10.

2) Shear and diagonal connections

a. Once the normal connections are defined and a certain Poisson ratio is adopted for the ballast sample (from experiments or literature), the linear properties of the shear and diagonal connections can be determined from Eq. (1).

b. The nonlinear properties of the shear and diagonal connections are determined from Eqs. (9) and (10) by imposing the friction angle ϕ_{fric} and the apparent cohesion c obtained from direct-shear test on ballast samples.

3) Correction of F_{ref}

a. Because F_{ref} was determined by using only the normal connection, this has to be corrected once the shear and diagonal connections are added. The correction is needed to ensure that $r_{\max}$ (as defined under point 1) is obtained for a cyclic load of amplitude F_{ref} (which is actually the definition of F_{ref}). The correction is proposed in Eq. (12) and contains a correction factor η. This factor needs to be tuned such that the final settlement ($r_{\max}$) is obtained for F_{ref}. A tuning example is given in Figure 9 where $\eta = 2$ seems to lead to best results. For other lattice parameters the lines shown in Figure 8 may be different; these lines can be calculated for the new parameters, and η leading to the best fit can be chosen.

Appendix B

The values of parameters adopted for the simulations in Section 0 are summarized in tables in this appendix. More detailed motivation of the choice of parameters values is given in Section 0 .

Table 1
Parameter values (*The small value used for the contact stiffness is explained in Section 5.1 and in Appendix C).

Category	Parameter	Symbol	Value	Units
Rails	Bending stiffness	EI_{rail}	12.05×10^6	Nm^2
	Linear mass	m_{rail}	120	kg/m
Sleepers	Mass	M_s	315	kg
	Rotational inertia	J_s	4.73	kgm^2
Rail pads	Vertical stiffness	K_v	10^8	N/m
	Rotational stiffness	K_θ	2.14×10^5	Nm
	Vertical damping	C_v	10^5	Ns/m
	Rotational damping	C_θ	2.14×10^2	Nms
Under-sleeper pads	Stiffness	K_{usp}	1.72×10^8	N/m
	Damping	C_{usp}	1.72×10^5	Ns/m
Vehicle	¼ Car body mass	M_c	8250	kg
	½ Boogie mass	M_b	2500	kg
	Wheelset	M_w	1700	kg
	Primary suspension stiffness	k_p	3426×10^3	N/m
	Primary suspension damping	c_p	36×10^3	Ns/m
	Secondary suspension stiffness	k_s	656×10^3	N/m
	Secondary suspension damping	c_s	18×10^3	Ns/m
	Contact stiffness	k_c	$2.4 \times 10^{9*}$	N/m

Table 2
Parameter values of the lattice representing the ballast layer.

Category	Parameter	Symbol	Value	Units
Ballast	Characteristic distance	d	0.03	m
	Mass	m^{lat}	4.05	kg
	Stiffness of normal connection	$k^{\mathrm{lat}}_{\mathrm{normal}}$	120×10^6	N/m
	Damping of normal connection	$c^{\mathrm{lat}}_{\mathrm{normal}}$	120×10^3	Ns/m
	Stiffness of shear connection	$k^{\mathrm{lat}}_{\mathrm{shear}}$	12×10^6	N/m
	Damping of shear connection	$c^{\mathrm{lat}}_{\mathrm{shear}}$	12×10^3	Ns/m
	Stiffness of diagonal connection	$k^{\mathrm{lat}}_{\mathrm{diag}}$	54×10^6	N/m
	Damping of diagonal connection	$c^{\mathrm{lat}}_{\mathrm{diag}}$	54×10^3	Ns/m
	Stiffness 1 (see Figure 2)	k^{lat}_1	90×10^6	N/m
	Stiffness 2 (see Figure 2)	k^{lat}_2	30×10^6	N/m
	Stiffness 3 (see Figure 2)	k^{lat}_3	60×10^6	N/m
	Sliding force (see Figure 2)	$F^{1,\mathrm{lat}}_{2,\mathrm{max}}$	75	N
	Reference force (see Eq. (5))	$F^{\mathrm{lat}}_{\mathrm{ref}}$	6825	N
	Gap (see Figure 2)	g^{lat}_3	0.41×10^{-4}	m
	Maximum residual deformation	$r^{\mathrm{lat}}_{\mathrm{max}}$	0.73×10^{-3}	m
	Friction angle (see Eq. (8))	ϕ_{fric}	60.27	degrees
	Apparent cohesion (see Eq. (8))	c	9950	Pa

Table 3
Parameter values of the lattice representing the soil layer and the approach slabs.

Category	Parameter	Symbol	Value	Units
Soil	Characteristic distance	d	0.03	m
	Particle mass	m^{lat}	3.2	kg
	Stiffness of normal connection	$k^{\mathrm{lat}}_{\mathrm{normal}}$	140×10^6	N/m
	Damping of normal connection	$c^{\mathrm{lat}}_{\mathrm{normal}}$	117×10^3	Ns/m
	Stiffness of shear connection	$k^{\mathrm{lat}}_{\mathrm{shear}}$	0	N/m
	Damping of shear connection	$c^{\mathrm{lat}}_{\mathrm{shear}}$	0	Ns/m
	Stiffness of diagonal connection	$k^{\mathrm{lat}}_{\mathrm{diag}}$	70×10^6	N/m
	Damping of diagonal connection	$c^{\mathrm{lat}}_{\mathrm{diag}}$	58×10^3	Ns/m
	Bottom horizontal stiffness	k_h	1665×10^6	N/m
	Bottom horizontal damping	c_h	13.8×10^3	Ns/m
	Bottom vertical stiffness	k_v	1.77×10^6	N/m
	Bottom vertical damping	c_v	720	Ns/m
Approach slabs	Particle mass	m^{lat}	5.38	kg
	Stiffness of normal connection	$k^{\mathrm{lat}}_{\mathrm{normal}}$	3972×10^6	N/m
	Damping of normal connection	$c^{\mathrm{lat}}_{\mathrm{normal}}$	0	Ns/m
	Stiffness of shear connection	$k^{\mathrm{lat}}_{\mathrm{shear}}$	361×10^6	N/m
	Damping of shear connection	$c^{\mathrm{lat}}_{\mathrm{shear}}$	0	Ns/m
	Stiffness of diagonal connection	$k^{\mathrm{lat}}_{\mathrm{diag}}$	1806×10^6	N/m
	Damping of diagonal connection	$c^{\mathrm{lat}}_{\mathrm{diag}}$	0	Ns/m

Appendix C

In this appendix we show that the results obtained with a soft contact spring $k_c = 2.4 \times 10^9$ N/m (between wheels and rail) are qualitatively and quantitatively very similar to the ones obtained with the more generally used value $k_c = 2.4 \times 10^{11}$ N/m.

Figure 22 shows that the two responses match very well. The scenario of the approach slabs with a linear lattice is assumed, and an irregular profile equal to that obtained after 20 passages is used. As can be seen, there is no significant difference between the contact forces. The softer contact spring allows for a larger time step leading to significantly faster computations.

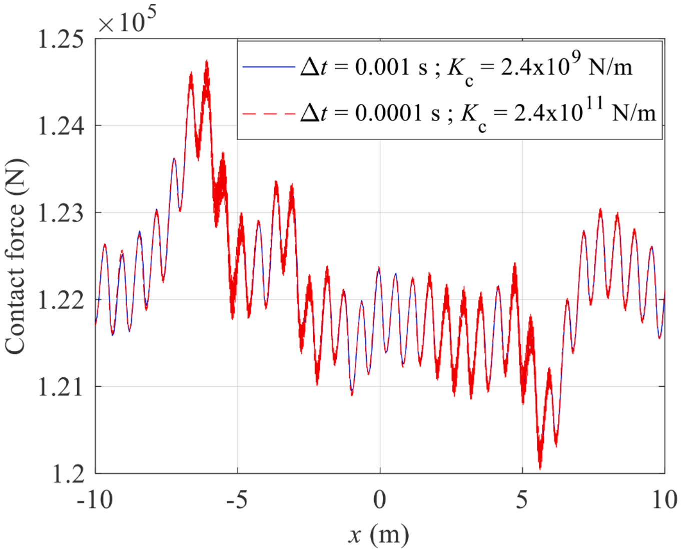

Figure 22. The contact force between the wheel and rail for two values of contact stiffness

References

[1] T. Dahlberg, Railway Track Stiffness Variations – Consequences and Countermeasures, Int. J. Civ. Eng. 8 (2010). http://ijce.iust.ac.ir/article-1-420-en.html.

[2] D. Li, D. Davis, Transition of railroad bridge approaches, J. Geotech. Geoenvironmental Eng. 131 (2005) 1392–1398.

[3] R. Sañudo, L. Dell'Olio, J. Casado, I. Carrascal, S. Diego, Track transitions in railways: A review, Constr. Build. Mater. 112 (2016) 140–157.

[4] W. Powrie, L. Le Pen, D. Milne, G. Watson, J. Harkness, Behaviour of under-track crossings on ballasted railways, Transp. Geotech. 21 (2019), 100258.

[5] J. Varandas, A. Paixão, E. Fortunato, A study on the dynamic train-track interaction over cut-fill transitions on buried culverts, Comput. Struct. 189 (2017) 49–61.

[6] M. Uranjek, A. Štrukelj, S. Lenart, I. Peruš, Analysis of influential parameters for accelerated degradation of ballast railway track, Constr. Build. Mater. 261 (2020), 119938.

[7] C.A. Ribeiro, R. Calçada, R. Delgado, Experimental assessment of the dynamic behaviour of the train-track system at a culvert transition zone, Eng. Struct. 138 (2017) 215–228.

[8] B. Coelho, P. Hölscher, J. Priest, W. Powrie, F. Barends, An assessment of transition zone performance, Proc. Inst. Mech. Eng. Part F J. Rail Rapid Transit. 225 (2011) 129–139.

[9] A. Paixão, E. Fortunato, R. Calçada, Transition zones to railway bridges: track measurements and numerical modelling, Eng. Struct. 80 (2014) 435–443.

[10] G.R. McDowell, W.L. Lim, A.C. Collop, R. Armitage, N.H. Thom, Laboratory simulation of train loading and tamping on ballast, Proc. Inst. Civ. Eng.-Transp. (2005) 89–95.

[11] A. Al Shaer, D. Duhamel, K. Sab, G. Forêt, L. Schmitt, Experimental settlement and dynamic behavior of a portion of ballasted railway track under high speed trains, J. Sound Vib. 316 (2008) 211–233.

[12] T.M. Čebašek, A. Esen, P.K. Woodward, O. Laghrouche, D.P. Connolly, Full scale laboratory testing of ballast and concrete slab tracks under phased cyclic loading, Transp. Geotech. 17 (2018) 33–40.

[13] T. Abadi, L.L. Pen, A. Zervos, W. Powrie, Improving the performance of railway tracks through ballast interventions, Proc. Inst. Mech. Eng. Part F J. Rail Rapid Transit. 232 (2018) 337–355.

[14] X. Zhang, C. Zhao, W. Zhai, C. Shi, Y. Feng, Investigation of track settlement and ballast degradation in the high-speed railway using a full-scale laboratory test, Proc. Inst. Mech. Eng. Part F J. Rail Rapid Transit. 233 (2019) 869–881.

[15] W. Lim, G. McDowell, Discrete element modelling of railway ballast, Granul. Matter. 7 (2005) 19–29.

[16] G. McDowell, O. Harireche, H. Konietzky, S. Brown, N. Thom, Discrete element modelling of geogrid-reinforced aggregates, Proc. Inst. Civ. Eng.-Geotech. Eng. 159 (2006) 35–48.

[17] M. Lu, G. McDowell, The importance of modelling ballast particle shape in the discrete element method, Granul. Matter. 9 (2007) 69.

[18] E. Tutumluer, Y. Qian, Y.M. Hashash, J. Ghaboussi, D.D. Davis, Discrete element modelling of ballasted track deformation behaviour, Int. J. Rail Transp. 1 (2013) 57–73.

[19] C. Chen, G.R. McDowell, An investigation of the dynamic behaviour of track transition zones using discrete element modelling, Proc. Inst. Mech. Eng. Part F J. Rail Rapid Transit. 230 (2016) 117–128.

[20] Y. Guo, C. Zhao, V. Markine, C. Shi, G. Jing, W. Zhai, Discrete element modelling of railway ballast performance considering particle shape and rolling resistance, Rail Eng. Sci. 28 (2020) 382–407.

[21] X. Zhang, C. Zhao, W. Zhai, Dynamic Behavior Analysis of High-Speed Railway Ballast under Moving Vehicle Loads Using Discrete Element Method, Int J Geomech 17 (2017), 04016157.

[22] W.M. Zhai, K.Y. Wang, J.H. Lin, Modelling and experiment of railway ballast vibrations, J. Sound Vib. 270 (2004) 673–683.

[23] A.B. Fărăgău, A.V. Metrikine, K.N. van Dalen, Transition radiation in a piecewise linear and infinite one-dimensional structure - a Laplace transform method, Nonlinear Dyn 98 (2019) 2435–2461.

[24] A.B. Fărăgău, T. Mazilu, A.V. Metrikine, T. Lu, K.N. van Dalen, Transition radiation in an infinite one-dimensional structure interacting with a moving oscillator - the Green's function method, J. Sound Vib. 492 (2021), https://doi.org/10.1016/j.jsv.2020.115804.

[25] A.B. Fărăgău, C. Keijdener, J.M. de Oliveira, A.V. Barbosa, K.N. Metrikine, van Dalen, Transition radiation in a nonlinear and infinite one-dimensional structure: a comparison of solution methods, Nonlinear Dyn 103 (2021) 1365–1391.

[26] M. Sadri, M. Steenbergen, Effects of railway track design on the expected degradation: Parametric study on energy dissipation, J. Sound Vib. 419 (2018) 281–301.

[27] M. Sadri, T. Lu, M. Steenbergen, Railway track degradation: The contribution of a spatially variant support stiffness-Local variation, J. Sound Vib. 455 (2019) 203–220.

[28] M. Sadri, T. Lu, M. Steenbergen, Railway track degradation: The contribution of a spatially variant support stiffness-Global variation, J. Sound Vib. 464 (2020), 114992.

[29] J. Alva-Hurtado, E. Selig, Permanent strain behavior of railroad ballast, 10th Int, Conf. Stockh. Swed. 1 (1981) 543–546.

[30] M. Shenton, Ballast deformation and track deterioration, Thomas Telford Ltd, London, 1985.

[31] Y. Sato, Japanese studies on deterioration of ballasted track, Veh Sys Dyn Int J Veh Mech Mob 24 (1995), https://doi.org/10.1080/00423119508969625.

[32] L. Mauer, An interactive track-train dynamic model for calculation of track error growth, Veh Sys Dyn Int J Veh Mech Mob 24 (1995), https://doi.org/10.1080/00423119508969626.

[33] J.N. Varandas, P. Hölscher, M.A. Silva, Settlement of ballasted track under traffic loading: application to transition zones, Proc. Inst. Mech. Eng. Part F J. Rail Rapid Transit. 228 (2014) 242–259.

[34] T. Dahlberg, Some railroad settlement models – a critical review. Proc IMechE Part F J Rail Rapid Transit, 2001, pp. 289–300, https://doi.org/10.1243/0954409011531585, n.d.

[35] A.S. Suiker, R. de Borst, A numerical model for the cyclic deterioration of railway tracks, Int. J. Numer. Methods Eng. 57 (2003) 441–470.

[36] J. Varandas, A. Paixão, E. Fortunato, B.Z. Coelho, P. Hölscher, Long-term deformation of railway tracks considering train-track interaction and non-linear resilient behaviour of aggregates–a 3D FEM implementation, Comput. Geotech. 126 (2020), 103712.

[37] A. Paixão, J.N. Varandas, E.C. Fortunato, Dynamic behavior in transition zones and long-term railway track performance, Front, Built Environ 7 (2021) 29.

[38] B. Indraratna, S. Nimbalkar, C. Rujikiatkamjorn, Stabilisation of ballast and subgrade with geosynthetic grids and drains for rail infrastructure (2011) 99–112.

[39] J.-Y. Shih, I. Grossoni, Y. Bezin, Settlement analysis using a generic ballasted track simulation package, Transp. Geotech. 20 (2022), 100249 n.d.

[40] K. Nguyen, D.I. Villalmanzo, J.M. Goicolea, F. Gabaldon, A computational procedure for prediction of ballasted track profile degradation under railway traffic loading, Proc IMechE Part F J Rail Rapid Transit 230 (2015) 1812–1827.

[41] S. Lobo-Guerrero, L.E. Vallejo, Discrete element method analysis of railtrack ballast degradation during cyclic loading, Granul. Matter. 8 (2006) 195–204, https://doi.org/10.1007/s10035-006-0006-2.

[42] E. Mahmoud, A.T. Papagiannakis, D. Renteria, Discrete Element Analysis of Railway Ballast under Cycling Loading, Adv. Transp. Geotech. 3 (2016) 1068–1076, https://doi.org/10.1016/j.proeng.2016.06.221.

[43] J.M. de Oliveira, K.N. Barbosa, van Dalen, Dynamic response of an infinite beam periodically supported by sleepers resting on a regular and infinite lattice: Semi-analytical solution, J. Sound Vib. (2019).

[44] J.M. de Oliveira, A.B. Barbosa, K.N. Fărăgău, van Dalen, A lattice model for transition zones in ballasted railway tracks, J. Sound Vib. 494 (2021), https://doi.org/10.1016/j.jsv.2020.115840.

[45] A. Suiker, A. Metrikine, R. De Borst, Dynamic behaviour of a layer of discrete particles, Part 1: Analysis of body waves and eigenmodes, J. Sound Vib. 240 (2001) 1–18.

[46] P.K. Woodward, J. Kennedy, O. Laghrouche, D. Connolly, G. Medero, Study of railway track stiffness modification by polyurethane reinforcement of the ballast, Transp. Geotech. 1 (2014) 214–224.

[47] A. Suiker, A. Metrikine, R. De Borst, Dynamic behaviour of a layer of discrete particles, Part 2: Response to a uniformly moving, harmonically vibrating load, J. Sound Vib. 240 (2001) 19–39.

[48] H.E. Stewart, Permanent strains from cyclic variable-amplitude loadings, J. Geotech. Eng. 112 (1986) 646–660.

[49] J.N.V. da S. Ferreira, Long-term behaviour of railway transitions under dynamic loading application to soft soil sites, (2013).

[50] W. Jia, V. Markine, Y. Guo, G. Jing, Experimental and numerical investigations on the shear behaviour of recycled railway ballast, Constr. Build. Mater. 217 (2019) 310–320.

[51] A.S. Suiker, E.T. Selig, R. Frenkel, Static and cyclic triaxial testing of ballast and subballast, J. Geotech. Geoenvironmental Eng. 131 (2005) 771–782.

[52] N.M. Newmark, A method of computation for structural dynamics, J. Eng. Mech. Div. 85 (1959) 67–94.

[53] S. Neves, A. Azevedo, R. Calçada, A direct method for analyzing the vertical vehicle–structure interaction, Eng. Struct. 34 (2012) 414–420.

[54] B.Z. Coelho, M.A. Hicks, Numerical analysis of railway transition zones in soft soil, Proc. Inst. Mech. Eng. Part F J. Rail Rapid Transit. 230 (2016).

[55] B. Zuada Coelho, J. Priest, P. Hölscher, Dynamic behaviour of transition zones in soft soils during regular train traffic, Proc. Inst. Mech. Eng. Part F J. Rail Rapid Transit. 232 (2018) 645–662.

[56] P.M.B.A. Costa, Vibrações do sistema via-maciço induzidas por tráfego ferroviário: modelação numérica e validação experimental, Univeristy of Porto, 2011. PhD thesis, https://repositorio-aberto.up.pt/bitstream/10216/61470/1/000148842.pdf.